JOURNAL OF GEOPHYSICAL RESEARCH: OCEANS, VOL. 119, 1–23, doi:10.1002/2013JC009278, 2014

Short-term upwelling events at the western African coast related to synoptic atmospheric structures as derived from satellite observations

F. Desbiolles,[1,2] B. Blanke,[1] and A. Bentamy[2]

Received 15 July 2013; revised 24 December 2013; accepted 26 December 2013.

[1] Satellite scatterometers provide continuously valuable surface wind speed and direction estimates over the global ocean on a regular grid both in space and time. The Level 3 data derived from the Advanced Scatterometer (ASCAT), available at 1/4° spatial resolution (hereafter AS25), and Quick Scatterometer (QuikSCAT), available on 1/2° and 1/4° horizontal grids (QS50 and QS25, respectively), are studied at regional scales in both the Benguela and Canary upwelling systems. They are compared to the European Center for Medium-Range Weather Forecast surface wind analysis, with insight into their intrinsic and actual spatial resolutions. In the coastal band, the finest spatial patterns are found in the QS25 winds and are O(75 km). This demonstrates the sensitivity of the high-resolution satellite-derived winds to coastal processes related to sea surface temperature (SST) perturbations and land-sea transition. Next, short-lived upwelling episodes (SUEs) calculated from SST anomalies are defined consistently with the QS25 actual resolution. These cold events refer to local, short-lived perturbations that add to seasonal upwelling variability. We characterize concomitant atmospheric synoptic conditions for SUEs identified at chosen latitudes and highlight two subregions in both upwelling systems, with contrasted patterns for the alongshore wind stress component and curl. The complexity of the latter patterns is closely linked to local, short-term SST variability. Closer to the shore, numerical sensitivity experiments show that the imbalance between Ekman transport and Ekman pumping has an impact on ocean dynamics: wind reduction in the coastal QS25 forcing, partially induced by orography, tends to reduce coastal SST cooling.

Citation: Desbiolles, F., B. Blanke, and A. Bentamy (2014), Short-term upwelling events at the western African coast related to synoptic atmospheric structures as derived from satellite observations, *J. Geophys. Res. Oceans*, *119*, doi:10.1002/2013JC009278.

1. Introduction

[2] Climate research programs do not limit themselves anymore to large-scale atmospheric and oceanic climate shifts. Regional impacts of climate change are demonstrated and ask for a thorough study of climate-biosphere interactions. In this framework, oceanic margins are a key field of investigation because they define a privileged link between continental fluxes and the open ocean. Therefore, the four major upwelling systems located on the eastern boundary of the Pacific and Atlantic oceans are a noteworthy issue. They represent only a few percent of the global ocean surface, but they supply about one-fifth of the marine catches [*Fréon et al*., 2009]. Some recent studies suggest the interrelation of climatic and oceanic environmental variability and regional ecology in eastern-boundary upwelling systems [*IPCC*, 2007]. These regions show a well-defined spatial extension and, therefore, they are interesting laboratories for the study of oceanic processes near continental margins and interactions between the ocean and the overlying atmosphere.

[3] Several studies connected the dynamics of an upwelling zone with spatial structures in the wind observed at fine scale and high frequency [*Carr*, 1998; *Pickett and Paduan*, 2003; *Blanke et al*., 2005], such as in the Saint Helena Bay (the most important nursery area in the Benguela upwelling system). Additionally, airborne experimental studies have been implemented in eastern-boundary upwelling systems to describe the role of fine-scale wind patterns on typical upwelling events [*Münchow*, 2000]. More precisely, the orography-induced wind stress curl has an effect on the fine dynamics scales of the upwelling circulation. This phenomenon is confirmed by numerical experiments that show high oceanic sensitivity to the spatial organization of the wind stress curl, particularly in a narrow band close to the seashore [*Capet et al*., 2004].

[4] The sea surface temperature (SST) distribution influences surface winds through thermodynamical and dynamical, local and remote feedbacks [e.g., *Chang and Philander*, 1994], over short time scales (of the order of a

[1]Laboratoire de Physique des Océans, UMR 6523 CNRS-Ifremer-IRD-UBO, Brest, France.
[2]Laboratoire d'Océanographie Spatiale, Ifremer, Centre de Brest, Brest, France.

Corresponding author: F. Desbiolles, Laboratoire de Physique des Océans, UMR 6523 CNRS-Ifremer-IRD-UBO, 29200 Brest CEDEX, France. (fabien.desbiolles@univ-brest.fr)

2169-9275/14/10.1002/2013JC009278

few days) because of the fast dynamical adjustment between the two fluids. For instance, atmosphere cooling over cold water increases the stratification of the air column, stabilizes the atmospheric marine boundary layer, and thus decreases both vertical turbulent mixing and convection. This process uncouples the surface winds from the more intense flow at elevations above the top of the planetary boundary layer, and increases the vertical wind shear near the sea surface. *Chelton et al*. [2004, 2007] and *Haack et al*. [2008] have demonstrated the importance of this feedback in structuring the winds over specific upwelling SST patterns. The parameterization of the wind-SST feedback in an ocean model can help reduce the biases related to the inshore extrapolation of satellite wind observations near the coast via wind reduction associated with colder SST, as shown by *Jin et al*. [2009] for the northeastern Pacific Ocean. In return, this decrease in coastal wind intensity allows reducing the intensity of the upwelling and of the cold bias usually modeled at the coast. The result is a modification of the coastal current system linked to the upwelling dynamics.

[5] A specificity of wind-SST interaction in eastern-boundary upwelling systems also stems from the interplay of a nearby coastline, fine scales in the wind, and the thermal surface signature of the upwelling process, especially in the cross-shore direction. SST and surface wind fields often show pronounced gradients over the first dozens of kilometers of the coastal ocean. The gradients appear as an upwelling front for SST and a dropoff zone for the wind [*Pickett and Paduan*, 2003; *Capet et al*., 2004]. The resulting wind curl produces Ekman pumping that contributes significantly to the structuring of the upwelling [*Bakun and Nelson*, 1991; *Halpern*, 2002]. According to topography, interaction of oceanic mesoscale features and wind-SST interaction, the horizontal scales can fall down to a few kilometers. In a recent study, *Fennel et al*. [2012] studied the sensitivity of the Benguela upwelling system to horizontal scales in the wind stress, and especially to the wind stress curl, both numerically and theoretically. They showed that the small scales of the wind shape the full three-dimensional circulation. In return, mesoscale SST perturbations influence the wind over the whole extension of the upwelling [*Chelton et al*., 2007]. Coupled air-sea processes in eastern-boundary upwelling systems were addressed by *Boé et al*. [2011] and *Renault et al*. [2012] for the California and the Humboldt systems, respectively. In addition to this coupling, forcing processes induced by orography and coastline geometry influence the wind over a coastal transition zone that may extend more than 100 km offshore [*Boé et al*., 2011].

[6] Therefore, quality momentum fluxes are essential ingredients to model accurately the ocean circulation in upwelling zones. *Burls and Reason* [2008] discussed some systematic biases between observations and model data reported by *Penven* [2000] in the Southern Benguela system, and attributed them to poorly resolved wind variability in the model atmospheric forcing (wind data from a coarse resolution climatology in this instance). They stressed the need for higher-resolution products able to sample mesoscale variability in the wind stress near the coast. Such data can be expected from meteorological models, following the standard analyses by the National Centers for Environmental Prediction (NCEP) and European Center for Medium-Range Weather Forecasts (ECMWF) with typical average resolution of a few tens of kilometers and 6 h in time. Even higher-resolution products begin to be produced, with, for instance, a change of the resolution of the ECMWF deterministic operational model to 16 km on 26 January 2010. It is worth noting that these momentum fluxes are modeled quantities and are not calculated directly from in situ or remote-sensed data sets. Moreover, surface wind calculations by meteorological models imply the use of high-performance marine boundary layer models that rely on semiempirical calibrations and parameters.

[7] During the last two decades, significant improvements in surface wind observations (for speed and direction) over the global ocean have been achieved. They are mainly retrieved from scatterometers such as the European Remote Sensing Satellites (ERS1/2), Advanced Scatterometer (ASCAT), and Quick Scatterometer (QuikSCAT). The measurements of ERS1/2 and QuikSCAT scatterometers have allowed a better description of surface winds and, therefore, led to improvements in numerical simulations performed with ocean models. Today, the Centre National d'Études Spatiales (CNES), European Space Agency (ESA), and European Organisation for the Exploitation of Meteorological Satellites (EUMETSAT) deal with space missions involving new scatterometer instruments, aiming at a global fine spatial and temporal resolution (25 km daily, or even 12.5 km). This resolution gets closer to the conditions needed for the correct derivation of space and time properties of wind-sea interactions in eastern-boundary upwelling systems. Some key limitations of the satellite wind retrievals are still worth noting such as inadequate temporal sampling of fast atmospheric variability and data contamination by the land-ocean transition and by rain, which reduces the overall number of reliable observations.

[8] In this study, we investigate the genuine horizontal resolution of recent global wind stress products by diagnosing spatial scales of covariability in QuikSCAT, ASCAT, and ECMWF winds over the Benguela and Canary upwelling systems (section 2). Once evidenced the synoptic variability in satellite-derived wind products (and especially wind reduction over the upwelling extension), we use jointly SST and wind daily maps to connect short-lived cold events over the continental shelf and synoptic wind patterns (section 3). In section 4, we investigate the ocean response to an alteration of the coastal wind stress equivalent to an orographic dropoff by means of twin experiments run with a regional ocean model. Our conclusions are discussed in section 5.

2. Actual Space Resolution of Global Wind Products in Upwelling Regions

2.1. Context

[9] The Atlantic Ocean is under the influence of large-scale atmospheric systems that are linked to the sea level high-pressure patterns shown in Figure 1. Air within the Azores and Saint Helena anticyclones flows to the intertropical convergence zone (ITCZ). At the African coast, therefore, equatorward trade winds make upwelling-favorable conditions in both the Canary and Benguela

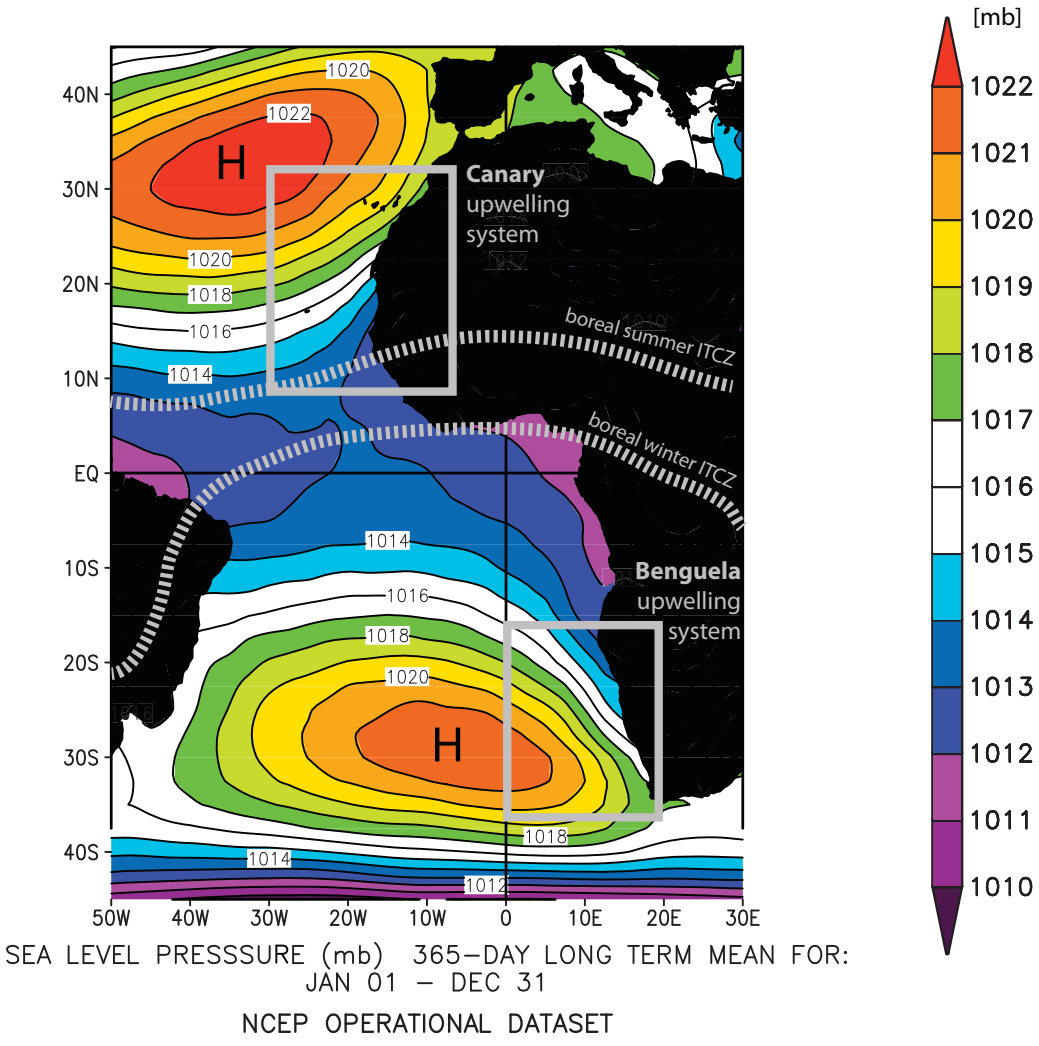

Figure 1. Mean annual surface air pressure (in mb) over the Atlantic Ocean deduced from 2005 NCEP data. Our domains of study are framed in gray and cover the Canary and Benguela upwelling systems. The approximate ITCZ mean positions during boreal summer and winter are indicated with gray dotted lines. The background map was downloaded from the NOAA web server (http://www.esrl.noaa.gov/psd/data/histdata/).

upwelling systems. The seasonal shift of the ITCZ and both anticyclones over the Atlantic translates in modulations of the coastal upwelling [*Wooster et al*., 1976].

[10] Geostrophic winds calculated by large-scale atmospheric models have long been used to study the variability of the upwelling systems [*Bakun*, 1973; *Schwing et al*., 1996]. However, as discussed by *Enriquez and Friehe* [1995] and *Pickett and Paduan* [2003] for the California system, large and fine-scale wind effects on the coastal ocean circulation have an equivalent order of magnitude. Coastal water divergence induced by large atmospheric scales and Ekman pumping processes induced by smaller wind scales generate comparable vertical fluxes in the ocean. Upwelling limitation by onshore geostrophic flow is also to be considered, especially for matching SST-based upwelling indices [*Marchesiello and Estrade*, 2010]. Recent work pioneered by *Estrade et al*. [2008] and extended by *Marchesiello and Estrade* [2010] investigated meticulously the various scales at play for a better quantification of the upwelling mechanism. The dynamical response of an upwelling system to specified winds must be differentiated according to the atmospheric scales at play, keeping in mind that both land orography and coastal geometry impact the wind stress curl responsible for Ekman pumping. The cross-shore scale of the wind dropoff and the genuine offshore scale of the coastal upwelling (which depends on the geometry of the shelf) are essential quantities to consider to distinguish between Ekman pumping- and Ekman transport-induced vertical movements [*Estrade et al*., 2008]. *Renault et al*. [2012] recently investigated this issue in their study of the upwelling response to atmospheric variability off central Chile, in the case of a very narrow shelf. Moreover, cold SST conditions during an established upwelling episode can decrease the overlying winds by acting on the stability of the atmospheric boundary layer, and, therefore, modify the wind stress curl over the SST gradients [*Jin et al*., 2009].

[11] For the past 20 years, outstanding efforts have been made in the description and understanding of the atmospheric conditions at the sea surface. An increasing number of space missions and major technical improvements have allowed refinement of the space and time resolution of the products available at global scale. Satellite scatterometers continuously provide valuable surface wind speed and direction observations over the global ocean. Since 2007, high spatial resolution wind retrievals are derived from ASCAT onboard MetOp-A. They are routinely used to estimate daily global wind fields with a spatial resolution of 0.25° in longitude and latitude (L3 products) [*Bentamy and Croizé-Fillon*, 2011]. Moreover, new L3 products derived from the updated QuikSCAT observations (hereafter QS25) and developed at the Institut Français de Recherche pour l'Exploitation de la Mer (Ifremer) are available with the same spatial and temporal characteristics as ASCAT L3 products. In this study, we aim at investigating the genuine horizontal resolution of 10 m wind analyses from these two new data sets, especially through comparisons with ECMWF surface wind analyses and former daily QuikSCAT L3 products (hereafter QS50). Technical considerations specific to each instrument, such as the geometry and frequency of the signals, are not discussed here but can be found in *Bentamy and Piollé* [2004]. More specifically, details about ASCAT and QuikSCAT wind retrieval, quality control, and validation procedures may be found in *Verhoef and Stoffelen* [2010] and *Dunbar et al*. [2006].

[12] The ECMWF data we use are the daily means of the zonal and meridional wind analyses available at the synoptic hours of 00:00, 06:00, 12:00, and 18:00 UTC from the Integrated Forecasting System (IFS) operational global atmospheric model. The model was run at T511 resolution (equivalent to a grid size of approximately 40 km) during our period of study (2000–2009). It is worth reminding here that the IFS assimilates satellite-derived wind data, and especially QuikSCAT and ASCAT observations. The assimilation of QuikSCAT data became operational on 22 January 2002. For the purposes of our study, the ECMW wind data are gridded at global scale with a resolution of 0.5° in latitude and longitude.

[13] Our analysis focuses on the two main eastern-boundary upwelling systems off the African west coast (the Benguela and Canary systems, see Figure 1) during upwelling-favorable wind periods (in January to February and July to August, respectively). Our main objective is to characterize the genuine horizontal resolution of remotely sensed and numerical model winds (surface wind stress, wind curl, and divergence, and, in a near future, heat fluxes) that proves essential in air-sea interactions at regional and local levels. Cross-correlation analyses and classical statistical calculations are used for that purpose.

2.2. "Intrinsic" Spatial Resolution

[14] QuikSCAT data are available from October 1999 to November 2009, whereas ASCAT data are available since April 2007. ECMWF analyses are available over both periods and, as already stated, result from a scheme that assimilates satellite wind data. The processing is done at the Centre ERS d'Archivage et de Traitement (CERSAT), located at Ifremer, provides L3 satellite products with 1/4° (ASCAT and QS25) or 1/2° (QS50) spatial resolution. Including ECMWF outputs (1/2°), four different data sets are thus available over a whole year (2008) for analysis (Table 1).

Table 1. Characteristics of the Global Wind Products Under Study

Products	QS50	QS25	AS25	ECMWF
Sources	QuikSCAT	QuikSCAT	MeTop-A	Model
Revisit time (days)	4	4	4	n/a
Orbital period (min)	101	101	101	n/a
Intrinsic resolution (°)	1/2	1/4	1/4	1/2

[15] Despite differences between the ASCAT and QuikSCAT radar physics and retrieval methods, the processes used to calculate L3 satellite-derived products are based on the same methodology. Scatterometer retrievals (L2 products) are used to estimate daily global gridded wind fields with horizontal resolution of 0.25° both in longitude and latitude [*Bentamy and Croizé-Fillon*, 2011]. The resulting gridded fields, labeled as L3 products, distinguish wind speed, the zonal and meridional wind components, wind stress, and the associated wind stress components. These quantities are calculated separately for ASCAT and QuikSCAT. Details of the objective method used for daily scatterometer analysis and estimate of its accuracy are provided in *Bentamy and Croizé-Fillon* [2011]. In brief, daily gridded wind speed, zonal, and meridional wind components are estimated, over 0.25°-grid cells in longitude and latitude, from scatterometer retrievals. Only valid remotely sensed data are selected, according to quality control flags associated with scatterometer products. For instance, scatterometer measurements occurring over wind vector cells partially over land or ice are not used for daily analysis calculation. Rain-contaminated data are also excluded. Daily gridded wind fields derived from former QuikSCAT L3 products and from ECMWF, both with a resolution of 0.50° in longitude and latitude, are also used in this study to investigate the improvements possibly allowed by finer spatial resolution of the surface wind field.

[16] The *k*-nearest neighbor (kNN) algorithm [*Mitchell*, 1997] is hereafter applied on each data set to derive gridded meridional and zonal wind components on the exact same stencil (25 km × 25 km squares), without altering their intrinsic resolution. Our analysis of wind variability focuses on 2 months of upwelling-favorable atmospheric conditions, i.e., January 2008 to February 2008 and July 2008 to August 2008 for the Benguela and the Canary systems, respectively (see section 2.3). Figure 2 shows the mean (colored arrows) and standard deviation (contours) of the wind vector in the Benguela upwelling area for each wind product. All products show consistent similarity during austral summer: the wind vector is mostly favorable to upwelling, i.e., northward and northwestward, over the whole domain. The maximum intensity is reached at about a hundred of kilometers offshore with a decrease in wind magnitude near the coast, except in the Lüderitz upwelling cell (27°S–25°S) where maximum variability occurs. Equivalent results are found for the Canary upwelling system over July to August: in average, the wind vector is similar for all the products, and the maximum of wind and

Table 2. Typical Parameter Values for, From Left to Right, the Coriolis Parameter, Temperature, and Depth of the Surface Mixed Layer, Subjacent Stratification, Reference Density, Acceleration Due to Gravity, Horizontal Scale of the Wind Perturbation, Wind Stress Perturbation, Reference Wind Stress, and Total Rate of Surface Mixed Layer Forcing by the Wind-Wave Field

f (s^{-1})	T_{ml} (°C)	H_{ml} (m)	T_z (°C/m)	ρ_0 (kg/m^3)	g (m^2/s)	δx (m)	$\Delta\tau$ (Pa])	τ (Pa)	γ
7×10^{-5}	15	10	0.2	1026	9.81	50×10^3	0.2	0.2	10

wind variability at the coast is obtained near Cape Blanc (21°N), noting that the Canary Islands are a source of topographic forcing that complicates the wind circulation leeward the archipelago. Finally, despite the consistency found in these products gridded at a regional scale, it is worth noting that L2 QuikSCAT wind speed retrievals

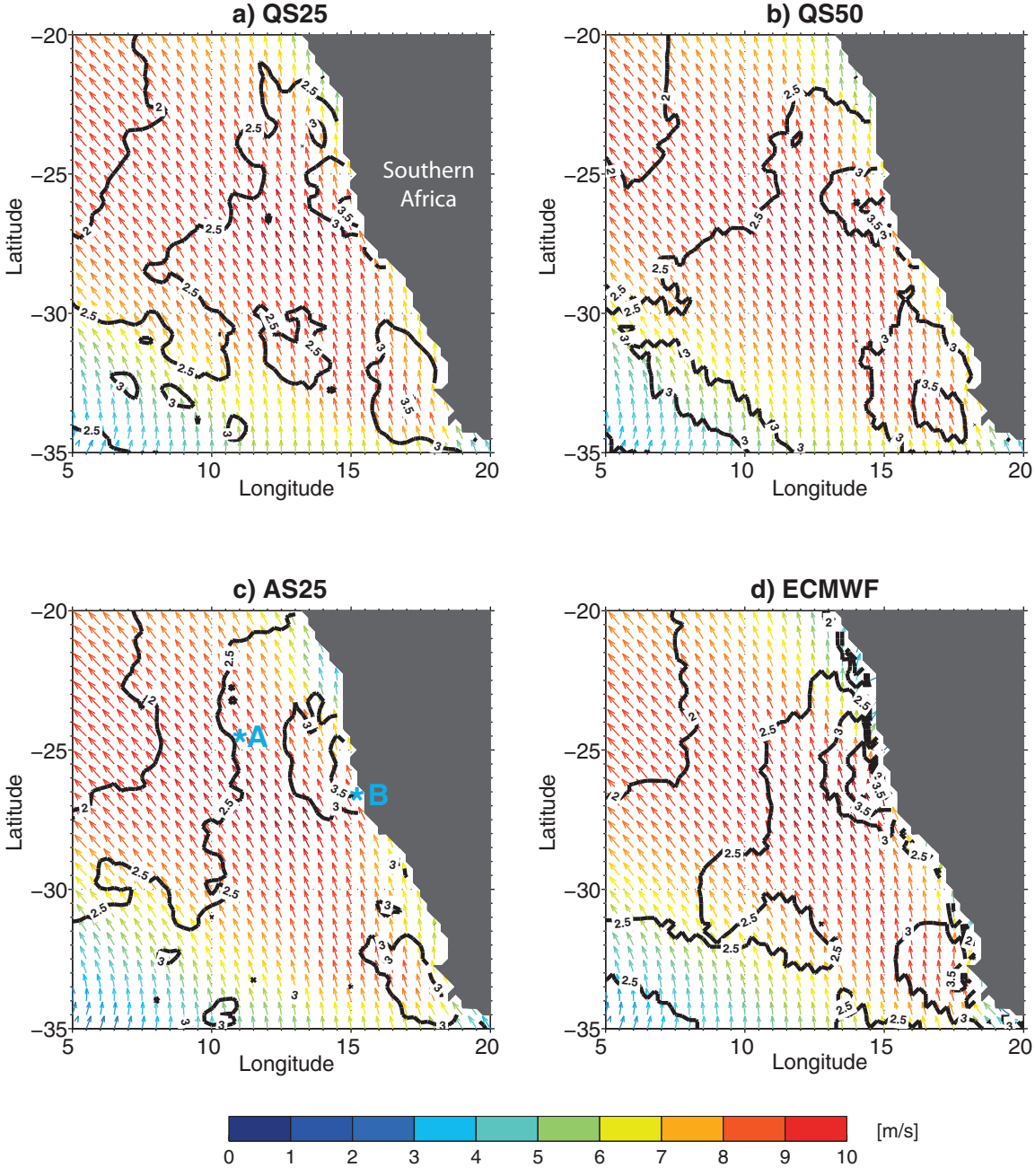

Figure 2. Mean wind vector (color) and standard deviation of wind speed (contours) for January to February 2008. (a) QS25. (b) QS50. (c) AS25. (d) ECMWF. Points A and B (discussed in the text) are shown in blue in Figure 2c.

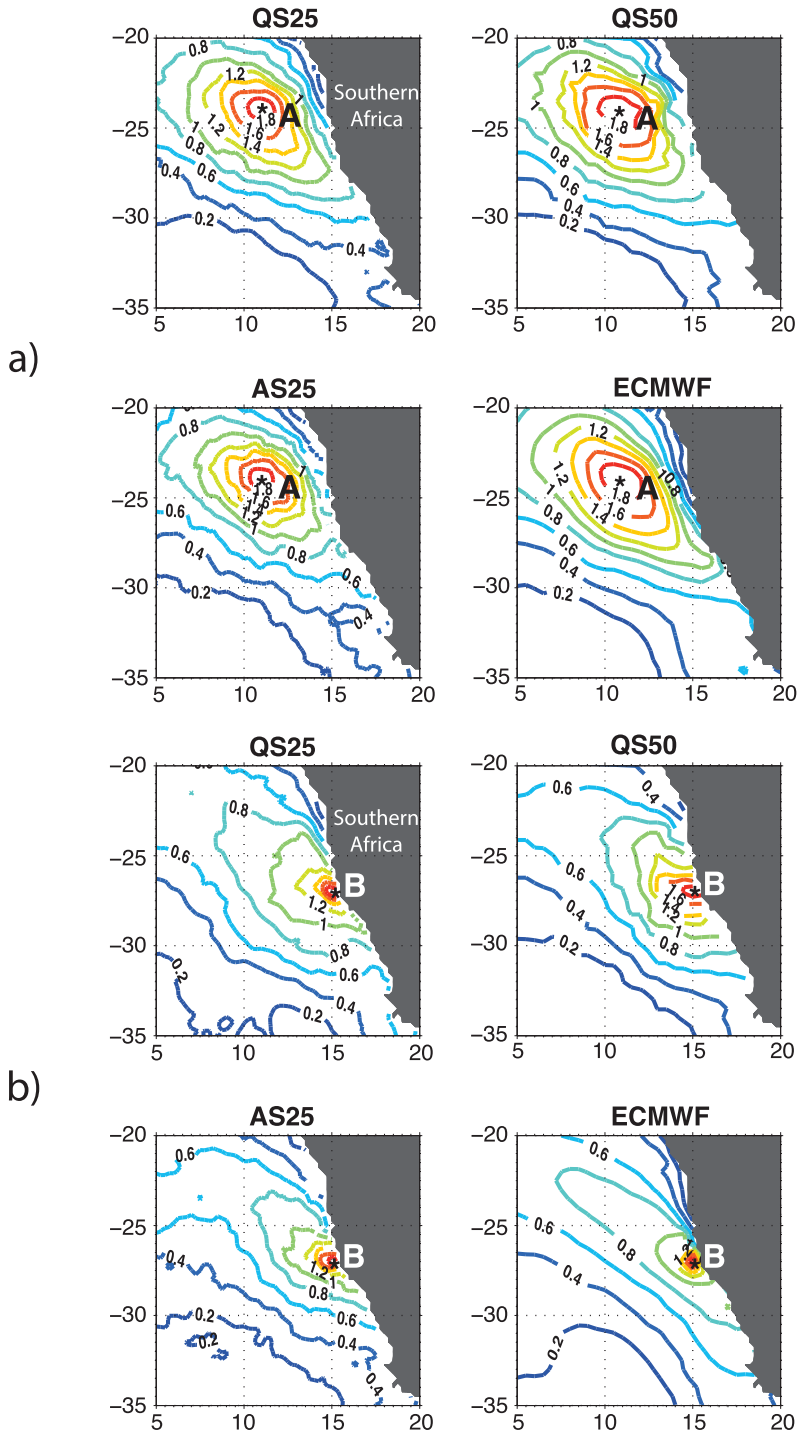

Figure 3. Vector correlation for the four wind products calculated with reference to the wind time series considered (a) at point A and (b) at point B.

have higher values than ASCAT estimates, especially in the 10–15 m/s wind speed range frequently observed for the trade winds [*Bentamy et al*., 2008].

2.3. Characterization of Actual Horizontal Resolution

[17] The wind spatial and temporal variability in the Benguela upwelling system is investigated at two locations: A (11°E–24.7°S) off South Africa and B (15°E–27°S) in the Lüderitz cell area (see Figure 2c). These sites are chosen for the strong and variable winds during the upwelling season (Figure 2) and characterize offshore and onshore wind variability, respectively. The assessment of the actual spatial resolution of each wind data set is based on cross-correlation analyses to estimate differences in horizontal homogeneity between the wind products.

[18] The vector correlation proposed by *Crosby et al*. [1993] provides a scalar measure of the agreement between two vector data sets with a coefficient that varies between

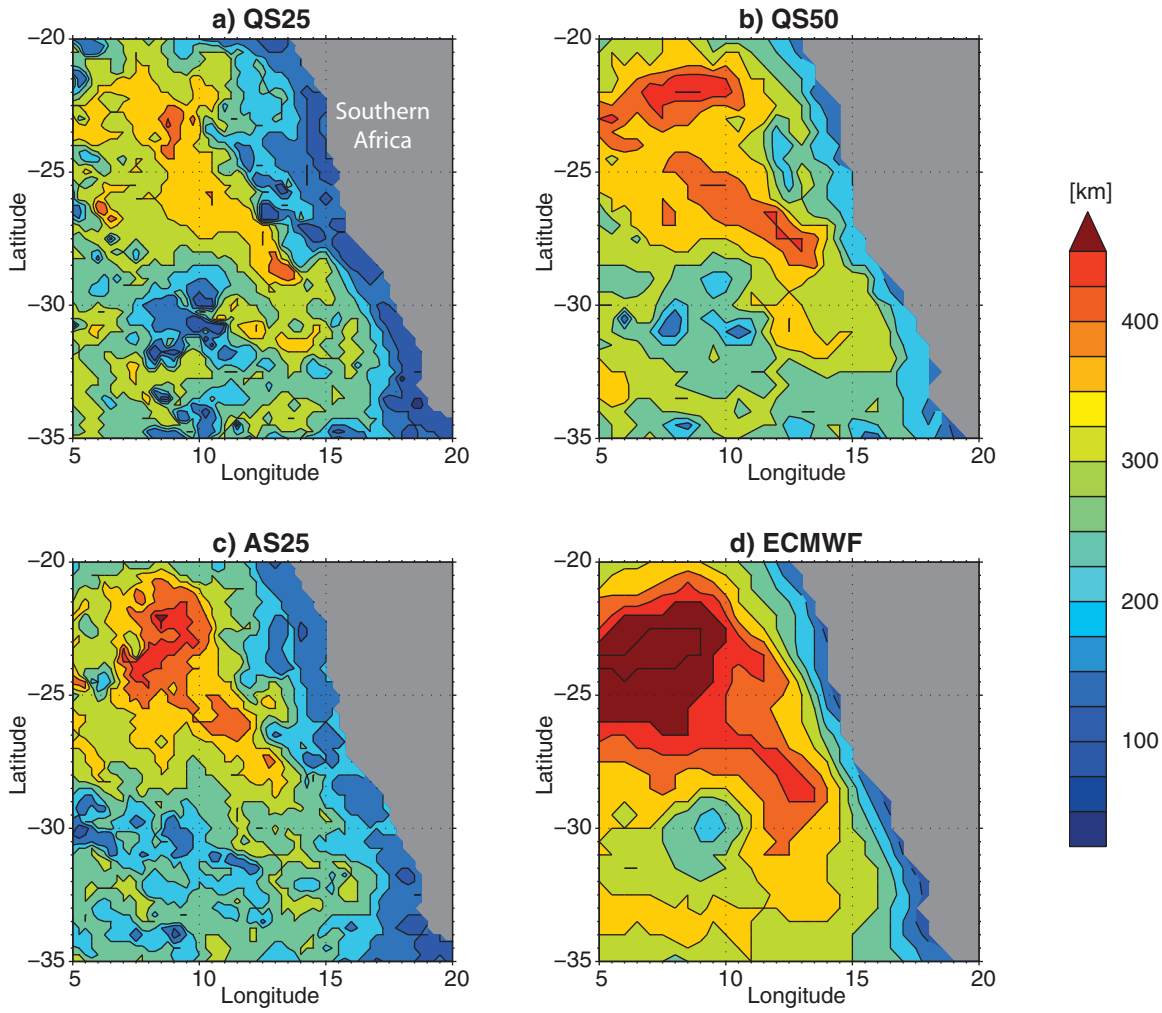

Figure 4. Distance (in km) at which the 0.95 threshold is reached in a cross-correlation analysis of the wind speed. (a) QS25. (b) QS50. (c) AS25. (d) ECMWF.

−2 and +2. We use the method to estimate the agreement between the zonal and meridional wind components of a reference time series at grid point A or B with the time series at all the grid points of the domain of study during January and February 2008. The result is a correlation coefficient that shows a dominant southeast-northwest wind structure during the austral summer season in the Benguela upwelling system (Figure 3). This pattern agrees well with the wind regime at this period of the year (see Figure 2): southerlies and south-easterlies occur most of the time and provide upwelling-favorable conditions along the western coast of Africa. Horizontal homogeneity in the wind is significantly smaller onshore, which underlines the importance of the ocean-land transition in modulating the wind components. The various wind sources exhibit quite similar spatial correlation patterns, highlighted in red. However, one should notice that the narrowest correlation scales in satellite data are derived from the new scatterometer products. This result especially stands out in the onshore area (B location) and shows finer atmospheric horizontal scales in the AS25 and QS25 products than in the former QS50 processing. The fine scales obtained for ECMWF wind data in the coastal zone result from the continuity of the wind calculation over the sea-continent transition, with differentiated parameterizations in the atmospheric model for the roughness length scales over ocean and land [*ECMWF*, 2007].

[19] Cross-correlation calculations are generalized over the whole domain for the wind speed. At each grid point, we compute the correlation coefficient between the local time series and the averaged time series of the four neighbors (north, east, south, and west) considered at a given and same distance (initially taken equal to 25 km). The computation is repeated with an increasing distance until the correlation coefficient becomes smaller than 0.95, and the corresponding distance is kept as the result of the analysis since it measures the local, horizontal coherence of wind intensity. The mean state and variability of the wind and the relative shortness of the period of analysis (see section 2.2) drive us into setting a high threshold to characterize wind consistency. In addition to the commonly used statistical significance, this threshold aims at considering the main physical processes that shape space-time wind variability in the coastal band. Indeed, we assume that these

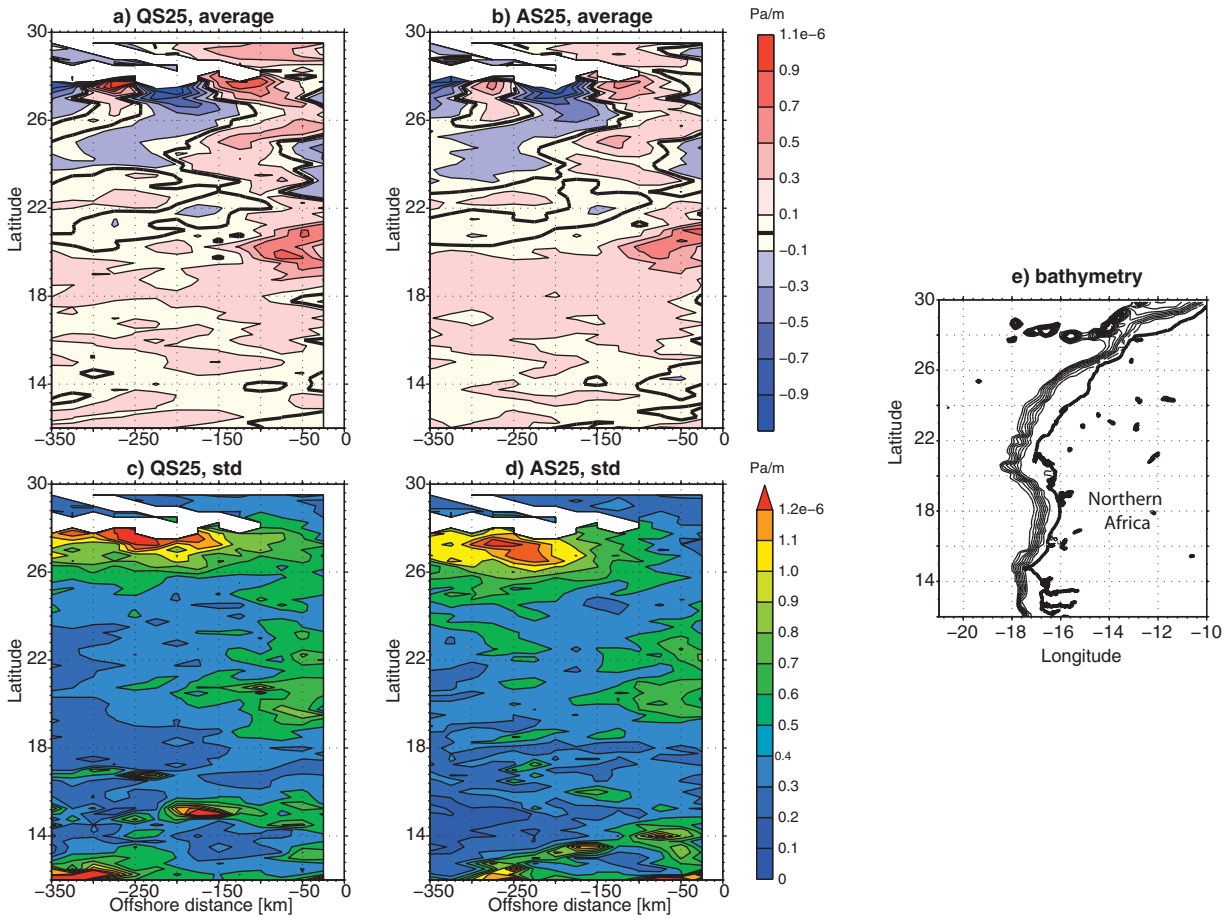

Figure 5. QS25 and AS25 wind stress curl (Pa/m) as a function of the distance to the coast in the Canary upwelling system. (a and b) July to August 2008 average for QS25 and AS25, respectively. (c and d) Standard deviation around the mean state for QS25 and AS25, respectively. (e) Coastline and bathymetry with a 250 m contour interval.

processes, namely SST mesoscale variations, coastline geometry, and orographic forcing (see section 1), generate significant spatial wind variability.

[20] The distance at which this threshold is reached is shown in Figure 4 and varies according to zones and products. However, the northern and to a lesser extent the southwestern parts of the domain show systematic high spatial correlations (distance larger than 300 km), whatever the source of data. These areas correspond to coherent wind data at large scale and can be easily associated with the Saint Helena anticyclone that steadily channels the winds equatorward. Satellite-derived winds (Figures 4a–4c) are associated with finer scales than model-derived winds since at equivalent intrinsic horizontal resolution the statistical threshold ($r > 0.95$) is satisfied in the model (Figure 4d) over larger distances. More precisely, the analysis of the QS25 and AS25 products underlines rather inhomogeneous regions, and especially the areas close to the coast where large air-sea-continent interactions are expected. The coastal wind dropoff and the wind modulation induced by SST gradients over the shelf indeed introduce short-scale variability in the coastal atmosphere and, therefore, sudden decrease of the correlation coefficient. Patterns of short-scale decorrelation are also found in the open ocean for both high-resolution products (Figures 4a and 4c). These structures in a southeast-northwest direction correspond to the main seasonal wind patterns identified in Figure 2 and highlight a large standard deviation of the meridional wind component (not shown).

[21] The actual spatial resolutions of the wind products stem from the analysis of the results shown in Figure 4. By comparison with QS50 and ECMWF, AS25 and QS25 show clearly the shortest correlation distances and, therefore, the finest spatial resolution. Moreover, in coastal areas (O(100 km) from the coast), the wind reduction induced by air-sea-continent interactions and orography is mainly captured by the QS25 product. Our analysis shows that the new satellite products have an actual horizontal resolution between 75 and 100 km and improve the representation of the cross-shore wind profile in comparison with QS50 (actual spatial resolution of about 150 km). Furthermore, it is worth noting that the mixing length values used in the ECMWF atmospheric boundary layer model are different according to how the calculations are done over the ocean or over the continent [*ECMWF*, 2007]. Therefore, land orography and coastal topography can modify locally the ECMWF analyses and account for substantial decrease in correlation spatial scales and wind speed (Figure 4d).

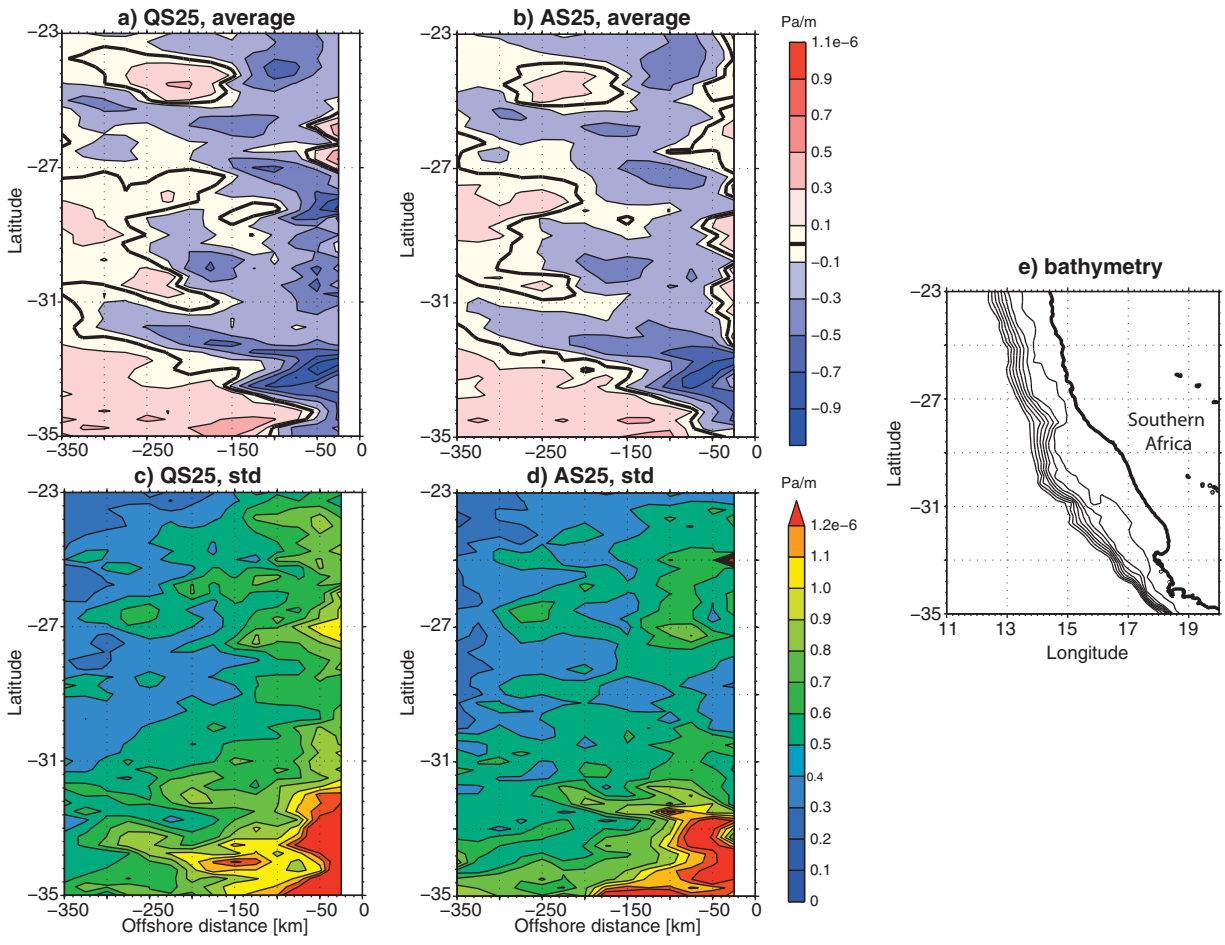

Figure 6. Same as Figure 5 but for the Benguela upwelling system and January 2008 to February 2008.

2.4. QS25/AS25 Comparison

[22] *Bentamy et al*. [2008, 2012] discussed in depth ASCAT-derived and QuikSCAT-derived wind quantities. The differences between ASCAT and QuikSCAT products are related to several parameters, including sea surface state, wind conditions, instrumental physics, wind retrieval algorithms, and spatial and temporal separations [*Bentamy et al*., 2008]. Over the global ocean, Level 2 and Level 2b swath data sets show persistent differences in colocalized wind intensities, whereas wind directions are coherent [*Bentamy et al*., 2008, 2012].

[23] For the gridded data sets (Level 3 products), small differences in wind features can produce a significant oceanic response. The alongshore wind stress, causing Ekman offshore transport, and the wind stress curl, causing upward or downward pumping, act on surface ocean structures, upwelling cells and circulation. For instance, *Fennel et al*. [2012] showed that the vertical structure of the coastal currents in the Benguela upwelling system responds strongly to alternating positive and negative wind stress curl, especially in the neighborhood of the continent.

[24] Figure 5 shows the mean and standard deviation of the wind stress curl as a function of the distance to the coast for the Canary upwelling system during summer 2008. An orographic-induced wind stress curl dipole can be identified north of 24°N. As demonstrated by *Mason et al*. [2011] in their numerical study, the sign and intensity of the curl play a key role in controlling the oceanic circulation and upwelling process leeward the islands and at the coast. In particular, they found that the offshore path of the Canary Current, north and across the archipelago, is sensitive to the nearshore variability of the wind stress curl, especially in the Lanzarote passage [see *Mason et al*., 2011, Figure 2b]. In this area, at about 75 km from the coast at 29°N, QS25 shows larger wind stress curl intensity and standard deviation than AS25 (Figure 5). South of 20°N, both wind products are characterized by the dominance of strong nearshore cyclonic curl, except at a few latitudes and especially downwind of Cape Verde (∼15°N). The positive upwelling-favorable wind stress curl (Figures 5a and 5b) takes up a large coastal band downwind of Cape Blanc (21°N), extending about 150 km offshore. Cape Blanc represents a source of topographic forcing for the summer wind stress curl with, therefore, negative (positive) values upwind (downwind) of the cape.

[25] In the Southern Hemisphere and on the large scale, the dominance of the trade winds is apparent and the QS25 wind stress is slightly more intense than AS25 over most of domain (Figures 2a and 2c). The main difference in wind stress curl is the presence of nearshore anticyclonic patterns in AS25 (Figure 6). The QS25 summer wind stress curl matches the description given by *Burls and Reason* [2008],

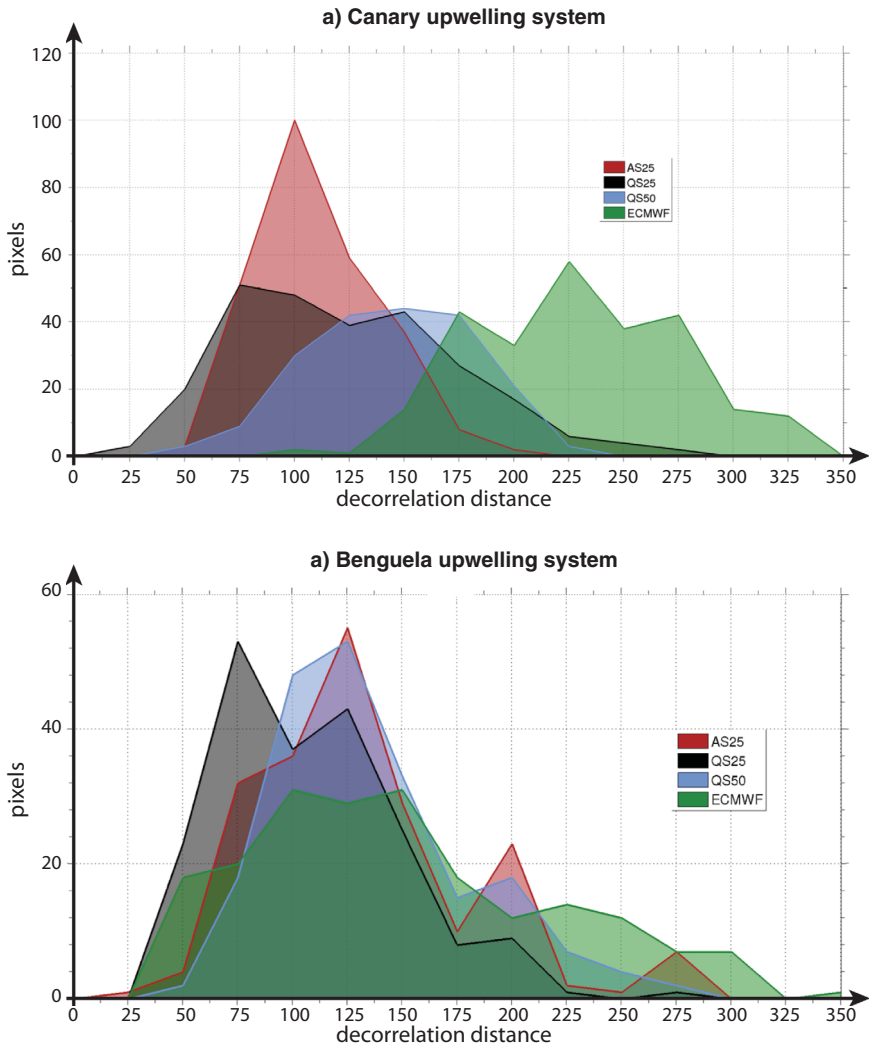

Figure 7. Number of pixels over the continental shelf in the cross-correlation analysis of the meridional wind stress component binned as a function of the decorrelation distance (with 25 km bins) for the four wind products. (a) For the Canary upwelling system. (b) For the Benguela upwelling system.

with a narrow coastal band of negative (upwelling favorable) curl that extends on average 75 km offshore but that may vary locally from 25 to 250 km. For both wind products, the largest extension is found downwind of Cape Columbine (33°S). It is worth noting that the largest upwelling-favorable curl, between 23°S and 25°S and between 28°S and 31°S, is not found at the coast but 50 to 100 km offshore. The Lüderitz upwelling cell centered at 26.5°S is characterized by positive wind stress curl at the coast, together with a large standard deviation (Figure 6c).

[26] In both Atlantic upwelling systems, the nearshore curl is expected to be related to topographical forcing induced by capes, as demonstrated in *Dorman et al*. [2013] for the California system. Inhomogeneities of the coastline, possibly combined with land orography, structure the upwelling dynamics [*Fennel et al*., 2012]. The above analysis shows that smaller structures are observed in the QS25 wind stress curl, with standard deviation values greater than in AS25. A few key latitudes also show that the wind stress curl variability and offshore extension are larger for QS25.

2.5. Interpretation

[27] To focus on the dynamical processes in the coastal band (over the continental shelf, i.e., for ocean depths within 0–500 m), we diagnose the spatial decorrelation scales of each product by counting the pixels belonging to distance bins ranging from 0–25 to 400–425 km now in the analysis of the meridional wind stress (i.e., in a way similar to the calculations done for Figure 4 but for the meridional wind stress component).

[28] Figure 7 shows the total number of such pixels (over 25 km square cells) for both the Canary and the Benguela continental shelves. For the Canary system, the two new wind data sets (AS25 and QS25) confirm the larger proportion of fine scales, with sharper curves centered on 100 km decorrelation distances (Figure 7a). The curves obtained for QS50 and ECMWF are smoother, and are centered on 175 and 300 km, respectively. The ECMWF scales of horizontal variability (Figure 7a, green area) confirm that orographic effects and the geometry of the coastline are of

limited importance along the shore of Northwestern Africa when compared to the Southern Hemisphere (Figure 7b). It is worth noting here that the actual resolution calculated with ECMWF data makes use of unmasked wind values over land. Therefore, the ECMWF winds are the product that shows the finest spatial scales for the Benguela system (Figure 7b). The coastline indeed acts as a topographic barrier and introduces significant spatial decorrelation in the wind maps. Among the satellite products and as expected, QS25 and AS25 winds show much finer spatial scales than those found resolved by QS50. It is also worth noting that QS25 presents shorter decorrelation distances than AS25 in both areas. The shorter revisit time of the QuikSCAT satellite and, thus, the larger number of data in the 25 km squares under the swaths can explain the smoother resolution in the AS25 winds [*Bentamy et al*., 2008].

[29] The two new surface wind data sets are available with an intrinsic horizontal resolution of 0.25° in longitude and latitude. Above the coastal waters, these products provide fine-scale two-dimensional wind fields with higher resolution than the previous QS50 and ECMWF products. The actual fine resolution of the new satellite data sets has the potential for improving the representation of coastal upwelling process in regional ocean models. The QS25 L3 product appears appropriately accurate for a thorough investigation of the upwelling dynamics along the west coast of Africa. Based on theoretical scales proposed by *Estrade et al*. [2008], *Veitch et al*. [2010] indeed put the width of the active coastal Ekman divergence in the Benguela upwelling system at 10–30 km, depending on the slope of the shelf (narrow shelf north of 20°S; broad shelf around 30°S), which is here of the order of one grid point (i.e., 0.25°) at the most. Ekman pumping related to the wind stress curl and to the possible wind dropoff at the coast spreads out over a larger distance (about 75 km), which suggests disconnection of both dynamical processes in the control of coastal SST variability [*Marchesiello and Estrade*, 2010].

[30] Moreover, vertical turbulent mixing induced by intensified local winds is also able to cool the sea surface by deepening the surface mixed layer and, thus, incorporating in it colder waters. The contribution of vertical mixing and vertical entrainment (i.e., Ekman pumping) to SST cooling stages was found of comparable significance in the numerical study carried out by *Renault et al*. [2012] for the central Chile upwelling system. A thorough investigation of this effect is not possible on the basis of satellite-derived surface fields alone, though a qualitative discussion can still be useful. The calculations provided in the Appendix A show that both effects can be diagnosed of similar magnitude on the SST, which is in keeping with the results proposed by *Renault et al*. [2012].

3. Analyses of Daily SST and Wind Stress Maps

3.1. SST Products

[31] SST is often used to study the variability of the coastal upwelling systems. On monthly time scales, atmospheric variability is held responsible for the alternation of cold and warm events [*Roy et al*., 2001; *Hardman-Mountford et al*., 2003], and a strong relationship between the coastal upwelling and the wind curl has been confirmed [*Van Camp et al*., 1991; *Santos et al*., 2005]. At short temporal scales, occasional small-scale upwelling events may occur at the coast under the influence of local wind variations [*Van Camp et al*., 1991]. This daily scale is important for a precise and consistent description of SST variability in upwelling areas [*Blanke et al*., 2005].

[32] Turbulent fluxes between the ocean and the atmosphere actively contribute to dynamical and thermodynamical variability in both fluids [*Ayina and Bentamy*, 2007]. Wind stress acts on surface ocean currents and provides energy for subsurface vertical mixing, which in return modulates SST and sea surface salinity (SSS) variability. Conversely, SST and—to a lesser extent—SSS control partially the turbulent fluxes at the air-sea interface. As fine knowledge is needed for these quantities, both over space and time, we use data sets derived from remotely sensed observations. Indeed, the remote sensing of wind and SST has the unique advantage of a continuous and quasi-synoptic coverage, unlike precious but too much scattered direct observations obtained from buoy networks and sea experiments.

[33] We use here the so-called Reynolds SST [*Reynolds et al*., 2007] over 2003–2009. It is a reconstruction by optimal interpolation of daily SST fields derived from two high-resolution satellite data sets: Advanced Very High Resolution Radiometer (AVHRR) and Advanced Microwave Scanning Radiometer (AMSR). One main advantage of the Reynolds SST is its full availability at the same intrinsic resolution as the momentum fluxes already introduced, with no missing data.

3.2. Search for Short-Lived Upwelling Events

[34] In both upwelling systems, we identify anomalous cold events by diagnosing first significant SST anomalies (1°C colder than mean climatological conditions) persisting for 3–7 days. This period corresponds to the build up of cold surface water in an idealized model forced by a constant alongshore wind stress and initialized by a homogeneous SST [*Wang*, 1997]. One should notice that such events are defined with respect to mean seasonal variability. Therefore, they are not strictly related to seasonal upwelling conditions, but rather to short-lived perturbations that add to the regular seasonal cycle. We assume here that, except at the peak of an upwelling season (when the coastal ocean is vertically homogenized), a subsurface vertical gradient exists in coastal temperature and allows synoptic wind variability to bring water colder than usual to the surface. The calculations are done per latitude, over a 500 km neighborhood from the coastline. Local climatological conditions correspond to the 7 year average of the low-passed SST time series with a 30 day running mean.

[35] Short-lived upwelling events (SUEs) are deduced from the anomalous cold events by adding the following requirement: the immediate neighborhood under study (two grid points northward or southward, or on either side, of the reference grid point; one grid point offshore) must also be labeled as a short anomalous episode for the same day. Therefore, the finest spatial scales of an SUE are 75 and 50 km in the alongshore and cross-shore directions, respectively. This spatial homogeneity is justified by the

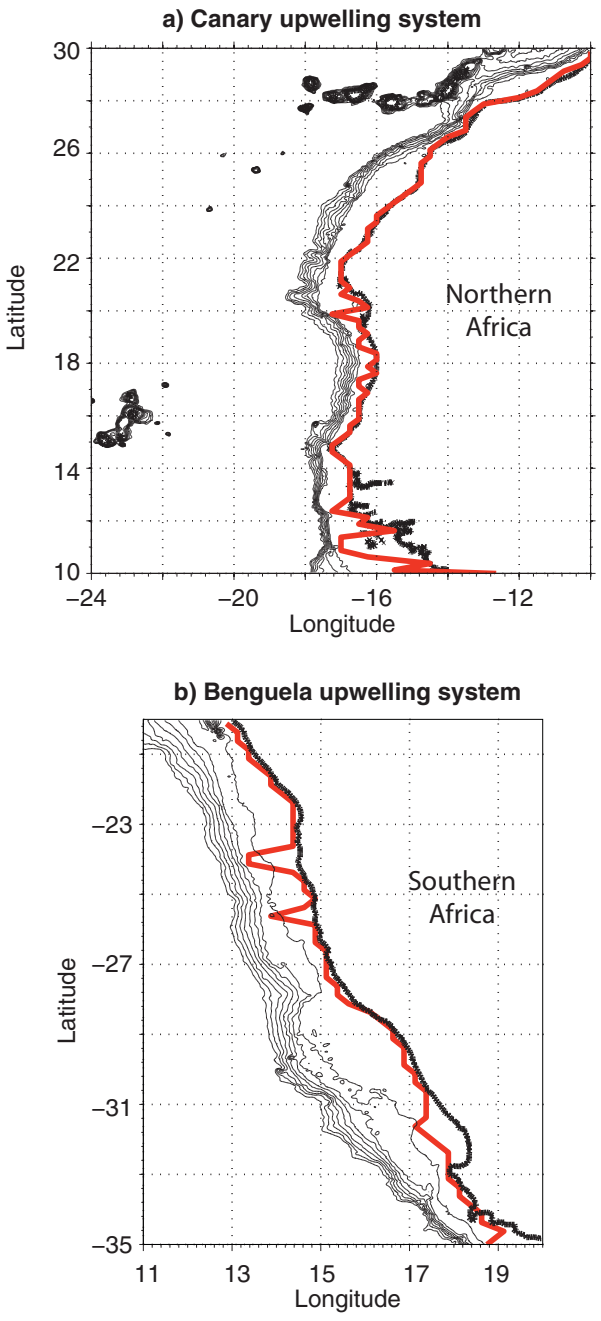

Figure 8. Bathymetry with black contours from 250 to 2000 m. The red line identifies the grid points that maximize at each latitude and over the shelf the number of SUEs. (a) For the Canary upwelling system. (b) For the Benguela upwelling system.

actual resolution found earlier in the QS25 products. We focus at each latitude on the SST grid point that captures most episodes over the shelf (red lines in Figure 8), defined here as inshore of the 500 m depth contour. Figure 8 shows that the number of SUEs is usually maximum at the coast, but it is worth noting that the complexity of the coastline and the structure of the continental shelf occasionally allow positioning of this maximum slightly offshore, a process usually observed on the leeward side of capes (i.e., Cape Blanc, at 21°N, Figure 8a; Cape Columbine, at 33°S, Figure 8b). According to *Estrade et al*. [2008] and *Dorman et al*. [2013], the location of the upwelling cell is influenced by the geometry of the shelf and coastline structuring of wind stress variability (see section 2.4), but also, to a lesser degree, by the density front delineating the tongue of the upwelled cold waters.

[36] In the next section, the SUE climatology for both systems is directly compared to the Ekman transport climatology at the reference grid points identified in red in Figure 8. The Ekman transport (expressed in m^2/s) is computed from the QS25 alongshore wind stress component with a beta-plane approximation centered on 20°N and 27°S for the Canary and Benguela systems, respectively. For the two areas, a negative (offshore) transport corresponds to upwelling conditions. A few key latitudes are discussed for each upwelling system, and will concentrate the rest of the analysis. Once the SUEs identified at these latitudes, we calculate composite maps for both the wind stress and SST as the average of both quantities over the dates corresponding to these anomalous events.

3.3. The Canary Upwelling System

[37] The climatic extension of the trade winds along the northwest coast of Africa is between 20°N and 34°N [*Hagen*, 2000]. Within these boundaries, the Canary Current and the North Equatorial Current are part of the northern Atlantic subtropical gyre and flow in geostrophic balance with the surface density gradient induced by the SST front that develops between the cold coastal waters and the warmer offshore ocean [*Allen*, 1973]. South of 20°N, the subtropical gyre is located offshore and a smaller, cyclonic, recirculation gyre occupies the inshore region. It shows poleward coastal currents and is under the influence of the equatorial circulation [*Mittelstaedt*, 1991; *Stramma et al*., 2005]. The meridional shift of the trade winds causes seasonal upwelling in this region, as shown by the Ekman transport climatology (Figure 9a). In line with the regional description proposed by *Lathuilière et al*. [2008], we will distinguish two subregions restricted to the subtropical gyre (22°N–30°N) and the recirculation gyre (10°N–22°N) because they are associated with specific patterns of space and time variability.

[38] Unlike the offshore Ekman transport, active almost all year long, the SUE seasonal climatology shows contrasted variability. The number and variability of SUEs vary indeed significantly with latitude (Figure 9b). Regions with poor activity of upwelling events, such as around 22°N and 27°N, come between regions of sustained SUEs. Offshore Senegal and Mauritania, from 10°N to 20°N, the southern subregion shows pronounced seasonal variability with a period of quasi-permanent SUEs from November to July and relaxation around September, in line with the seasonal meridional shift of the trade winds. The border zone between both subregions (around 22°N) is characterized by a small number of events (Figure 9c), but with permanent upwelling-favorable winds and, thus, sustained offshore transport throughout the calendar year. The northern subregion is associated with weaker seasonal variability and fewer cold events than its southern counterpart. SUEs are less frequent in summer although this is the season characterized with the strongest Ekman transport. The SUEs are

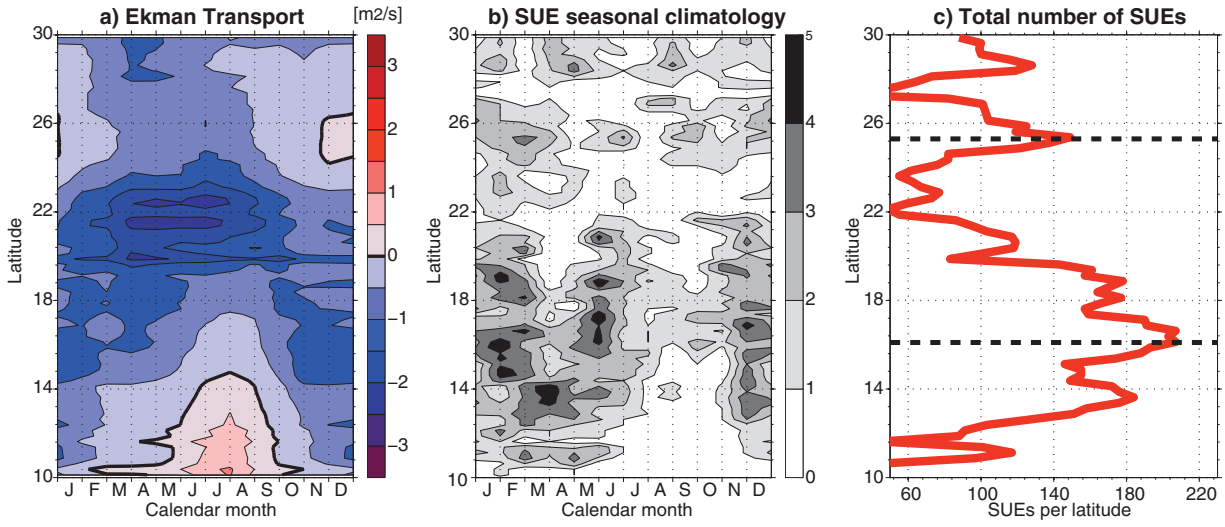

Figure 9. (a) Offshore Ekman transport (in m^2/s) seasonal climatology over 2004–2009 as a function of time (calendar month) and latitude. (b) SUE seasonal climatology over 2004–2009 as a function of time (calendar month) and latitude. (c) Total number of SUEs over 2004–2009 as a function of latitude. The bold dotted lines show the key latitudes selected for in-depth analysis.

therefore to be considered separately from the mean seasonal upwelling conditions in this region and are related to short-lived SST perturbations.

[39] In the subtropical gyre region, offshore Morocco and North Mauritania, a maximum number of SUEs are identified at 25.3°N. At this latitude, the upwelling process

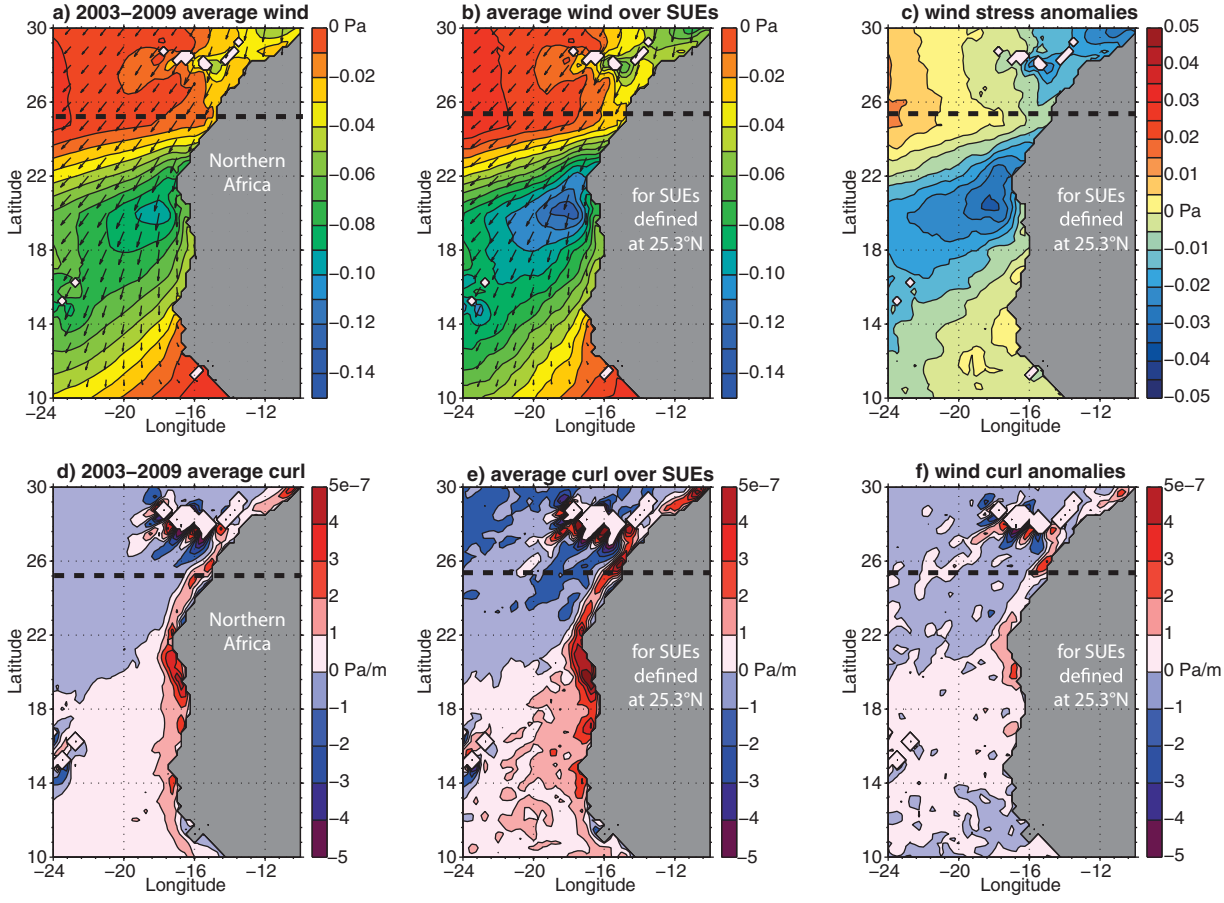

Figure 10. (top) Alongshore wind stress component and wind vectors and (bottom) wind stress curl, shown as (left) the average over 2003–2009, (middle) the composite average over the SUEs identified at 25.3°N, and (right) the corresponding anomaly. The reference latitude is shown with a thick dotted line.

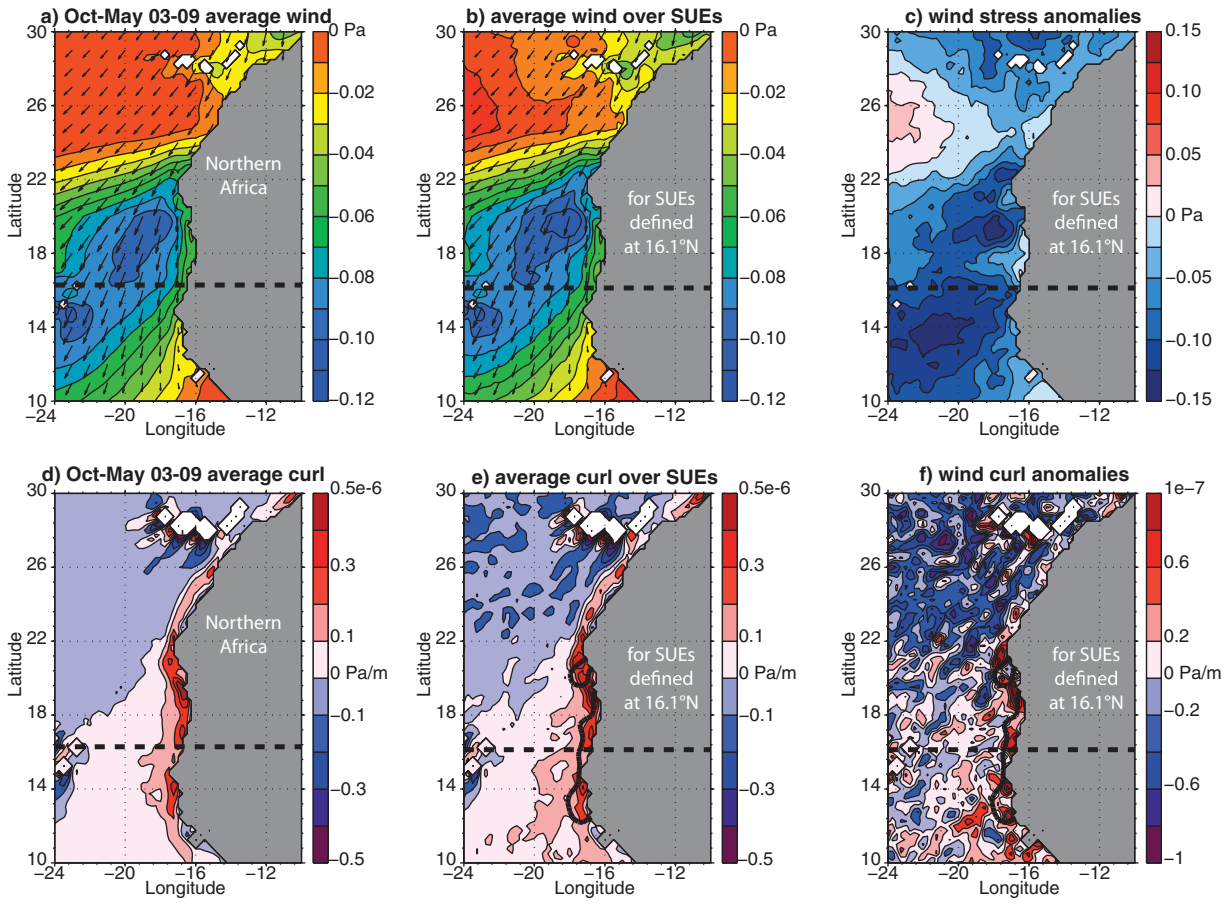

Figure 11. (a–c) Alongshore wind stress component and wind vectors and (d–f) wind stress curl, shown as (Figures 11a and 11d) the October-to-May average over 2003–2009, (Figure 11b and 11e) the composite average over the SUEs identified at 16.1°N, and (Figure 11c and 11f) the corresponding anomaly. The +1°C SST anomaly contour is added in Figures 11e and 11f, and the reference latitude is shown with a thick dotted line.

can be associated with both Ekman transport and Ekman pumping (Figure 10). Strong anomalies are found in composite images for the alongshore wind stress and the wind stress curl. The negative wind stress anomaly is present throughout the subtropical domain, with a maximum near the Canary Islands, because of wind channeling by island topography. Such atmospheric dynamics induces a succession of positive and negative wind stress curl downstream from the islands. A strong positive wind stress curl anomaly is also worth noting along the Lanzarote passage (see section 2.4). It activates Ekman pumping over the continental shelf at this latitude. Lastly, the Moroccan SUEs that can be detected all year long correspond to the combination of Ekman transport and pumping. A northerly wind pulse, channeled and accelerated near the Canary Islands, creates alongshore wind stress anomaly, favors offshore export of the coastal waters and accentuates the wind stress curl in the lee of the islands and alongshore (Figures 10d and 10e). Composite maps for these episodes indicate that SST anomalies confine to the Lanzarote passage (not shown).

[40] The recirculation gyre region shows stronger seasonality for the occurrence of SUEs, with a maximum number from November to June, and a relaxation period from July to October (Figure 9). This seasonality agrees with the variability of the Ekman transport and with former descriptions of the Canary upwelling system [*Hagen*, 2000; *Lathuilière et al.*, 2008]. Short-term wind variations add to seasonal variability in wind direction and intensity and may induce or suppress upwelling, which affects coastal dynamics. Figure 11 compares for this purpose the atmospheric synoptic fields during SUEs and standard upwelling conditions. The upwelling season in the recirculation gyre region (from October to April, Figure 9) is characterized by strong trade winds and an intense nearshore cyclonic wind stress curl (Figures 11a and 11d). The wind stress field during SUEs differs from this description with a stronger alongshore wind component in the border zone around 22°N and 20°N (Figure 11c). The cyclonic wind stress curl is strengthened during SUEs with values greater than the seasonal average alongshore Mauritania and Senegal (Figures 11e and 11f). Over this band of latitudes, the SUEs process is supported by strong trade wind anomalies around 22°N, i.e., with the amplification of the cyclonic wind stress curl near Cape Blanc along the coast of South Mauritania and Senegal. The SST anomaly takes up, therefore, the full coastal domain (black line in Figures 11e and 11f).

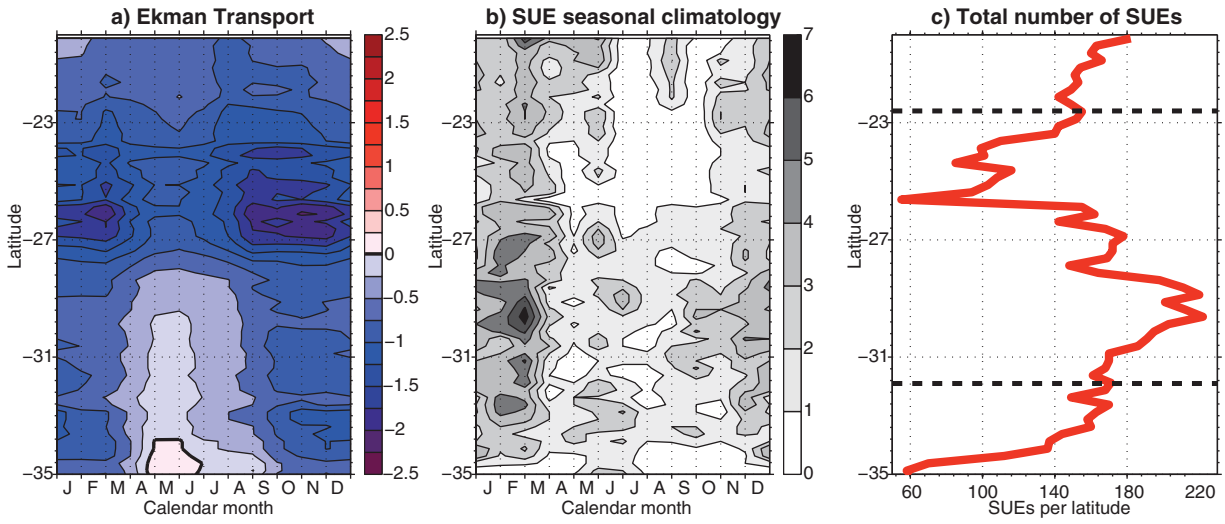

Figure 12. Same as Figure 9 but for the Benguela upwelling system.

3.4. The Benguela Upwelling System

[41] The Benguela upwelling system is usually divided into two subregions, separated at the latitude of the Lüderitz cell at 26.5°S. This environmental barrier can be explained with reference to biological and chemical processes, but also with reference to physical mechanisms [*Agenbag and Shannon*, 1988; *Shannon et al*., 2004; *Duncombe Rae*, 2005]. The atmospheric high-pressure system over the South Atlantic subtropical gyre channels strong trade winds along the western coast of South Africa. This system is modified at seasonal scales by pulses and southeastward migration of the zone of low pressure over the continent [*Tyson*, 1986]. This variability leads to upwelling-favorable winds during southern summer and during fall and spring in the Southern Benguela and Northern Benguela, respectively [*Duncombe Rae*, 2005]. *Agenbag and Shannon* [1988] showed that the atmospheric input of turbulent kinetic energy (thus of turbulent mixing) into the surface ocean layers lowers substantially north of 24.3°S. This effect is especially visible in the vertical profiles of temperature along the coast: the stratification is much stronger north of this latitude.

[42] Figure 12 shows the Ekman transport climatology and the climatology of the SUEs over 2003–2009 with their total number per latitude. The variability of the SUEs will be here studied at two latitudes of reference: 31.9°S (for the Southern Benguela) and 22.6°S (Northern Benguela). The seasonal cycle is strong over most of the domain. The southern summer (from December to March) is, however, the main season for offshore Ekman transport and the occurrence of cold anomalies. The boundary chosen to separate the Northern and Southern Benguela is justified by the small number of events diagnosed around 25°S although the offshore Ekman transport is almost maximum at this latitude (Figures 12a–12c). Though the mean seasonal climatology does not show significant contrasts between the two subregions, it is worth noting that only two out of 326 events are common to both areas. Therefore, Northern and Southern Benguela SUEs are not synchronous.

[43] This result is confirmed by significant differences found in the composite maps obtained for the alongshore component of the wind stress (Figure 13). For the Southern Benguela SUEs, a strong positive anomaly (favorable to upwelling) is found throughout the subdomain, but does not encroach on the coastal domain north of 25°S (Figure 13b). Conversely, an SUE in the Northern Benguela is associated with a localized anomaly of the alongshore wind stress (Figure 13c). For such episodes, the wind stress structure over the southern subdomain reflects anomalies of the zonal component of the wind stress, without significant meridional anomalies.

[44] The strong regional contrast in the organization of southern and northern SUEs is also noticeable in the composite maps calculated for SST (Figure 14). For both reference latitudes, SST anomalies essentially show regional patterns restricted either to the Southern or Northern Benguela subsystem. Southern Benguela SUEs are, however, characterized by a large meridional extent up to the Central Benguela, which is confirmed by a significant number of common (simultaneous) SUEs at 31.9°S and others latitudes in the southern area: the Southern Benguela shows some homogeneity in SST behavior from 33°S to 25°S, though wind stress patterns obtained for Central Benguela SUEs (not shown) suggest an atmospheric variability more localized than for Southern Benguela SUEs (Figure 13b). At all latitudes, positive anomalies of the alongshore wind stress components combine with negative anomalies of the wind stress curl, which means that both effects act on cooling SST. Note that, as initially proposed by *Marchesiello and Estrade* [2010] and *Veitch et al*. [2010] confirmed that the Bakun index (based on Ekman transport) must be corrected by a geostrophic contribution to reflect better the coastal upwelling dynamics in the Benguela upwelling system. The use of satellite altimetry for the derivation of such currents is, however, beyond the scope of our own study, and we are unable to assess the role of coastal convergence of geostrophic currents on activation or inhibition of SUEs.

4. Sensitivity of Coastal Dynamics to a Nearshore Wind Attenuation

[45] Thanks to their improved horizontal resolution, new satellite-derived wind products such as QS25 are able to

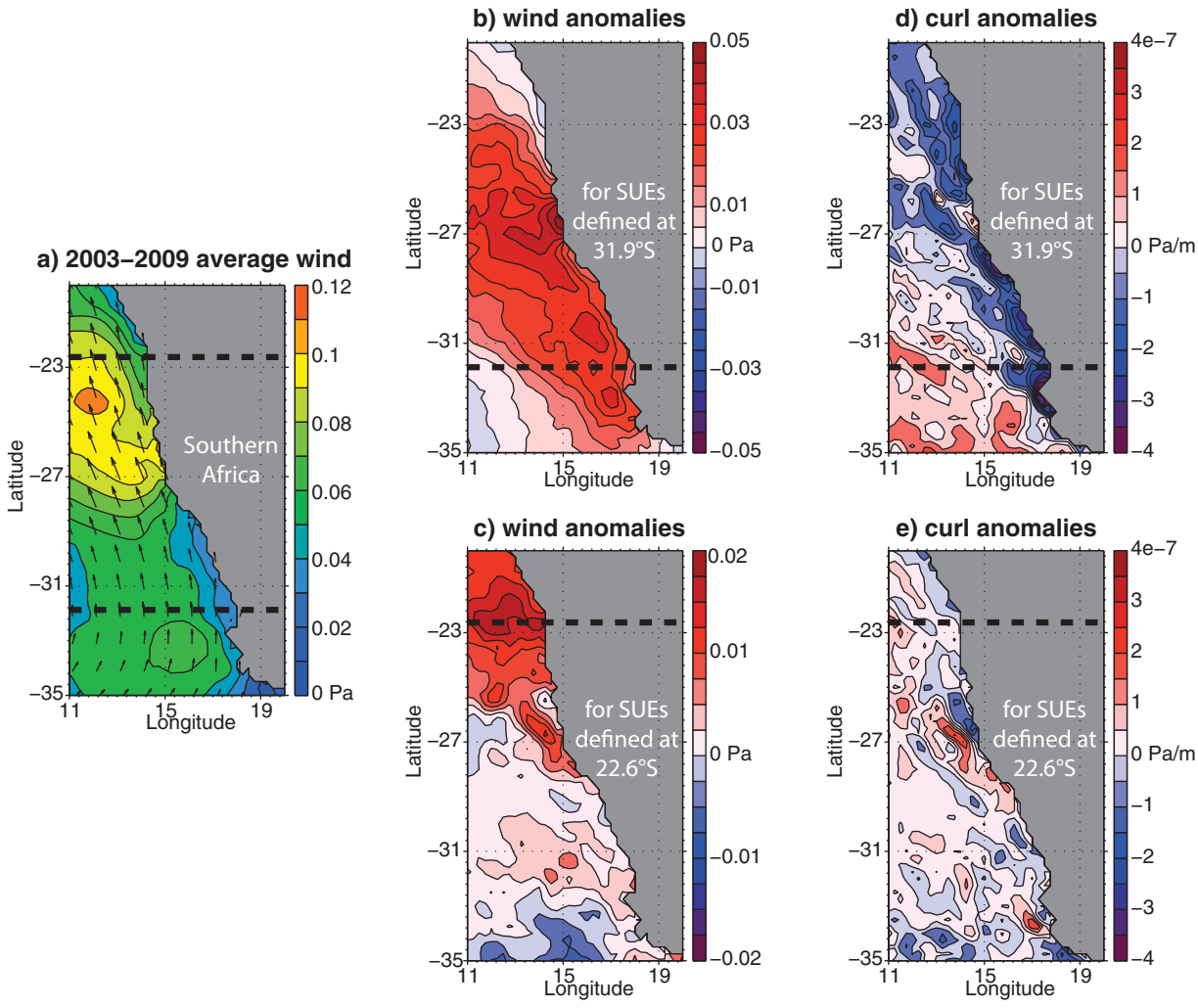

Figure 13. (a) Alongshore wind stress component and wind vectors averaged over 2003–2009. (b and c) Alongshore wind stress component averaged over the SUEs identified at 31.9°S (top) and 22.6°S (bottom) with respect to mean conditions. (d and e) Wind stress curl anomalies (in arbitrary units) averaged over the SUEs identified at 31.9°S (top) and 22.6°S (bottom) with respect to mean conditions. Both reference latitudes are shown with a thick dotted line in Figure 13a.

reproduce the wind reduction over the coastal ocean in eastern-boundary upwelling systems. However, the account of pure orographic wind dropoff is still a hard task because of the horizontal scales at play (a few tens of kilometers), especially in a blind zone for satellite scatterometers. In this section, we choose to investigate the sensitivity of the coastal SST to the fine scales of the dropoff by means of numerical experiments run with a regional ocean model. Ideally, we would add a wind dropoff—within the meaning of *Capet et al*. [2004]—at each latitude on the QuikSCAT wind stress, using the information (wind decrease) provided by a high-resolution atmospheric model. For the purposes of this study, however, we restrict our sensitivity tests to the scales that a wind product such as QS25 would capture in the absence of the coastal blind zone. In other words, we complete coastal gaps in QS25 with wind profiles derived from a product that does not have blind zone issues and that somehow accounts for coastal wind dropoff. To be consistent with the previous sections, we choose the ECMWF winds.

[46] We admit that the ECMWF product used in this study must be considered very carefully at the coastline because of possible numerical artifacts introduced by the land-ocean transition in the atmospheric model. It still defines a convenient correction to apply on the QuikSCAT winds for tests in a regional ocean model, knowing that the numerical experiments are not intended to reproduce the true ocean but are carried out as sensitivity studies. For the sake of brevity, our numerical tests are confined to the Benguela upwelling system and rely on the QS25 product. Note that the new generation of ECMWF analyses (starting from cycle 36r1 initiated on 26 January 2010) implements a significant upgrade in horizontal resolution (16 km). For comparison purposes, Figure 15 shows the meridional wind component in the Benguela upwelling system at 6:00:00 UTC on 3rd January 2011 at 1/2° and 9/64° resolutions. Over the open ocean, the increased lateral resolution does not change much the wind pattern. The nearshore wind attenuation is also equivalent in both analyses, with the notable exception of a very narrow coastal band where the

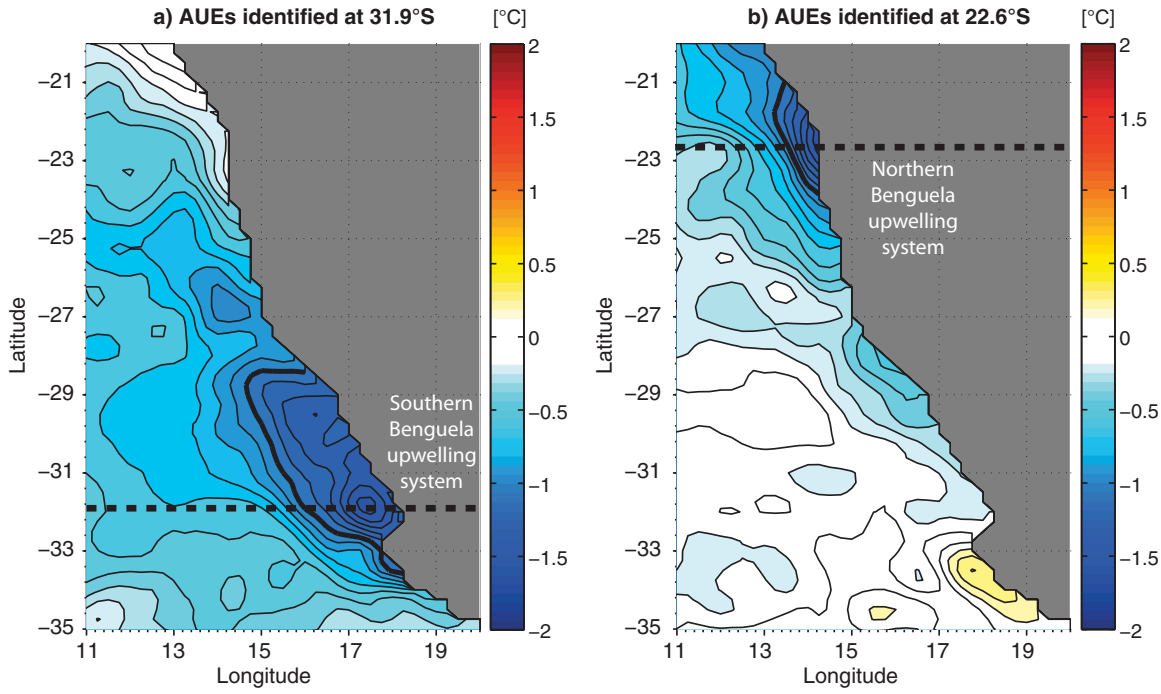

Figure 14. Composite maps of SST anomalies in the Benguela upwelling system. (a) For SUEs identified at 31.9°S. (b) For SUEs identified at 22.6°S. The −1°C SST anomaly contour is drawn as a bold line.

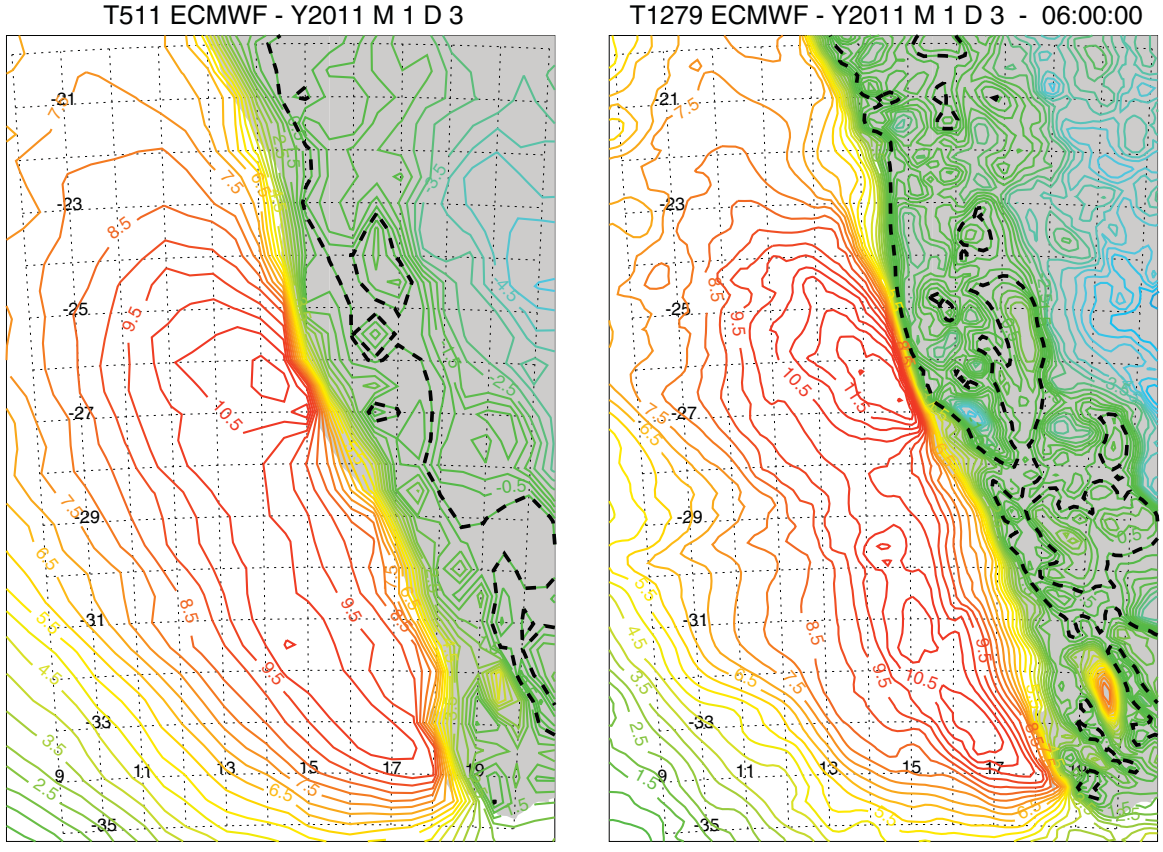

Figure 15. Meridional wind component on 3 January 2011, over the Benguela upwelling system from the IFS operational ECMWF spectral model. The contour interval is 0.5 m/s. (a) As a daily average for the T511 resolution. (b) At 06:00:00 for the T1279 resolution.

orographic dropoff occurs. At latitudes where wind attenuation is due solely to the ocean-land transition, such as 26.5°S, it is worth noting that the resolution of the 1/2° ECMWF product is not an obstacle to the reproduction of the deceleration, though with a larger cross-shore scale. At other latitudes, the coastal wind dropoff is likely diluted in the attenuation induced by SST-wind coupling.

4.1. The Numerical Framework

[47] We use the split-explicit, free-surface, primitive equations Regional Ocean Modeling System (ROMS), based on the Boussinesq approximation and hydrostatic vertical momentum balance [*Shchepetkin and McWilliams*, 2005, 2009]. The domain covers the ocean domain around Southern Africa from 38°S to 20°S and from 5°E to 22°E. The spatial resolution is 1/12° with 32 terrain-following vertical levels (with a higher resolution in the upper ocean layer). The bottom topography is derived from the ETOPO2 (2′ resolution) data set [*Smith and Sandwell*, 1997]. The simulation is initiated from rest, with temperature and salinity fields obtained from the World Ocean Atlas 2005 database [*Antonov et al*., 2006; *Locarnini et al*., 2006] monthly averages that are also used to constrain the model at its lateral open boundaries. The model is forced by fresh water and heat fluxes extracted from the Comprehensive Ocean-Atmosphere Data Set (COADS) ocean surface monthly climatology at 1/2° resolution. The model configuration is, therefore, quite similar to the one used by *Rimaud et al*. [2012], except its horizontal coverage. Here, the small size of the domain and the use of climatological fields as constraints on the model open boundaries cannot be regarded as optimal options to reproduce exactly the variability that can be observed over the continental shelf either with remotely sensed or in situ data. However, the numerical configuration is suitable for process-oriented studies based on sensitivity to the local atmospheric forcing, and the model sea level patterns are in fair agreement with that deduced from satellite observations of the surface elevation above the geoid height (not shown).

[48] In a first stage, the model is run for 21 years driven by a monthly climatological wind stress derived from daily QuikSCAT satellite scatterometer data gridded at 1/2° resolution (QS50, for the first 9 years) and 1/4° resolution (QS25, for the 12 following years). Then, the model is forced for 7 years with daily wind values corresponding to the repetition of year 2005. For the first 3 years of this second stage (years 22–24) we use genuine QS25 winds. In all these configurations, the QuikSCAT data are extrapolated toward the coast on the model ocean grid to fill the blind zone in radar scatterometer coverage. The last 4 years (25–28) introduce a coastal wind correction that allows a more thoughtful extension of the QS25 winds over the coastal blind zone and that may be interpreted locally as an orography-induced wind dropoff (see discussion of Figure 15).

[49] Specifically, the QS25 product, either for its climatology or for year 2005, is first extrapolated horizontally by nearest neighbor averaging and resampling to fill in missing values in the coastal ocean (but also onshore), and then interpolated on the finer ocean model grid. The ECMWF correction, more precisely the local zonal gradient in the ECMWF meridional stress component, is applied from the first (westernmost) missing grid cell in the nominal QS25 product. This gradient is extended eastward, without yet accepting a reversal of the component (in which case, the meridional wind stress is maintained at zero).

4.2. Twin Sensitivity Studies

[50] Our test experiments are 1 month long, focus on January 2005 and start from six different states that can be used for this purpose (end of years 22–27). For each initial state, the model is forced either with the genuine January 2005 QS25 wind product or with its modified version at the coast. By construction, 6 of the 12 experiments reproduce exactly, for 1 month, the trajectory of the model introduced in section 4.1. The other six experiments modify its trajectory because of the slight modifications introduced in the wind stress. The aim of the comparison is to identify the short-term (O(1 day or less)) signature of a wind dropoff on SST variability along the coast. The variety of initial states allows us to put in perspective the sensitivity to the dropoff and pure oceanic internal variability induced by submesoscale and mesoscale processes. Drawing initial states from either years 22 to 24 (genuine QS25 forcing) or years 25 to 27 (modified QS25 forcing) also helps us to vary the set of initial conditions by either applying a modified QS25 forcing after a long sequence of genuine QS25 forcing, or a genuine Q25 forcing after a sequence of modified QS25 forcing. Similar experiments were carried out over February 2005 to strengthen our conclusions and led to equivalent results (not shown).

[51] Our analyses focus on SST contrasts obtained after only 1 day of parallel integration (Figure 16). The differences on the longer term are harder to interpret because the modeled velocity field can transport SST anomalies away from their point of origin and make them unrelated to local wind differences. Moreover, our numerical framework does not account for any SST feedback on the atmospheric circulation and, therefore, is not suitable for long sensitivity tests. We checked that the sequence of forcing (genuine QS25 after modified QS25 or the other way around) does not alter the teaching that we can adopt concerning these twin experiments. This was not unexpected as the amplitude of the modification is weak compared to day-to-day variations of the wind stress. Then, it is worth mentioning that the signature in anomalous wind stress curl is not always negative: local positive values indicate that the cross-shore variability of the ECMWF wind stress can be associated instead with intensified winds at the shore line (i.e., do not show a dropoff). This is especially the case at 25.8°S and 30.6°S for the modification brought to the QS25 product both on 1st January and 1st February (Figure 16a).

[52] As reminded by *Renault et al*. [2012], negative anomalous curl at the coast will both decrease the cross-shore Ekman transport (over a characteristic cross-shore length scale related to the slope of the shelf) and increase Ekman pumping over the scale of the wind dropoff. The relative magnitude of both processes modulates the total upwelling velocity and, therefore, the signature in SST (Figure 16b), with the model's response modulated by the sharpness of the vertical and horizontal temperature gradients at the coastline, when considering upwelling or downwelling anomalies, respectively. The standard deviation of the SST response can locally exceed 0.25°C because

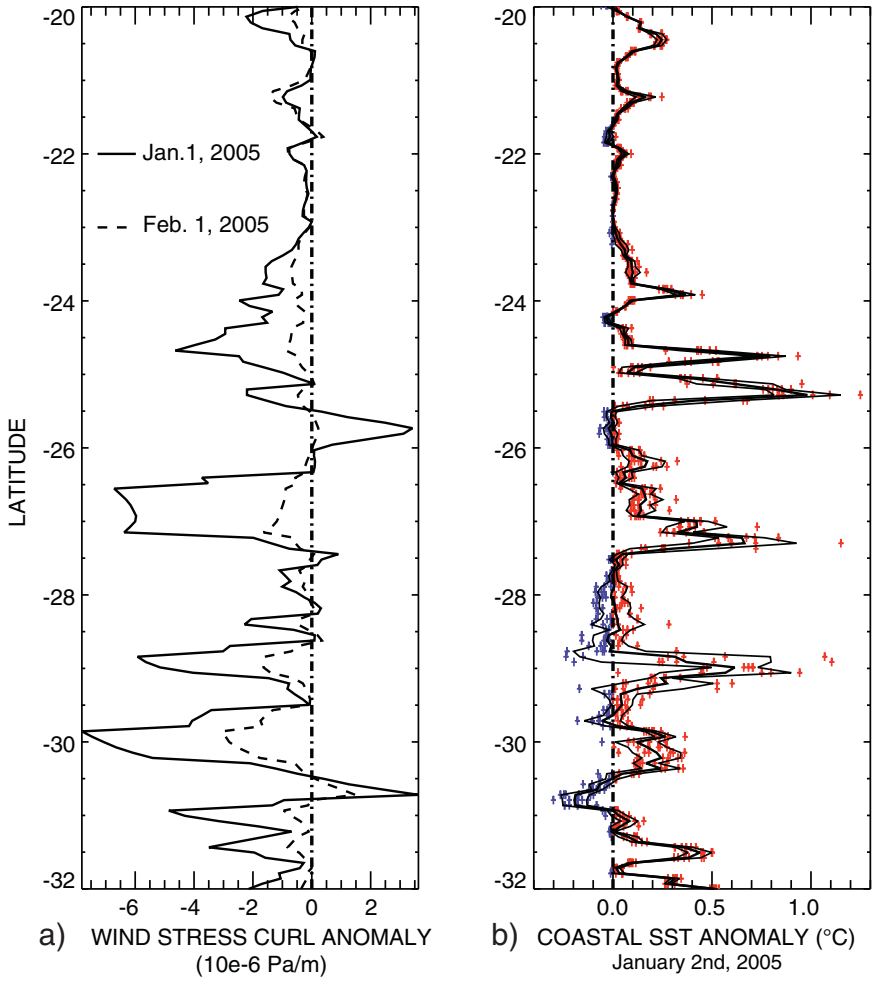

Figure 16. (a) Wind stress curl anomaly applied on the first day of January (solid line) and February (dashed line) 2005. (b) Coastal SST anomalies obtained after 1 day of six twin integrations over January 2005, with their mean and standard deviation drawn with solid and thin lines, respectively.

of sensitivity to mesoscale structures in the initial thermal field, and, at latitudes where the wind stress curl anomaly is only weakly negative, the SST anomaly can be of uncertain sign. Yet, for our twin experiments, the coastal SST is always warmed with the introduction of a coastal wind deceleration. This result appears consistent with a characteristic length scale of the coastal Ekman transport shorter than the scale of the wind dropoff.

5. Discussion and Conclusions

[53] In this study, high-resolution wind gridded data sets at 1/4° derived from QuikSCAT and ASCAT measurements (QS25 and AS25, respectively) with new wind retrieval algorithms developed at Ifremer were compared at regional and local scales in the Benguela and Canary upwelling systems with lower-resolution products at 1/2° (QS50 and ECMWF). QS25 and AS25 show finer spatial variability than the other products, especially in the coastal band, because of improved wind retrieval algorithms. Considering its sharper variability, QS25 was chosen as the reference product for the description of synoptic wind stress patterns during short-term upwelling events (SUEs). Wind stress variability and curl patterns were investigated nearshore where, in the cross-shore direction, several physical processes can alter the wind. In section 3, we mostly discussed the remote and local wind forcing of short-term SST anomalies identified at the coast or a little further offshore. Though the reciprocal impact of SST fronts on the wind stress curl was not fully discussed, our results show that the satellite-derived wind stress curl does increase over strong negative SST anomalies over the whole surface of the upwelling signature This supports the hypothesis that cross-shore SST gradients, potentially accentuated near the coast by SUEs, may expand the wind stress curl laterally [*Chelton et al*., 2007]. Closer to the shore, wind structures are also induced by the complexity of the coastlines and the presence of capes (Figure 5), and by the surface drag and atmospheric boundary layer at the land-sea interface [*Capet et al*., 2004; *Renault et al*., 2012]. This latter contribution was approached by the comparison of the actual resolution of satellite winds and ECMWF analyses in onshore areas (section 2). Moreover, numerical twin experiments carried out with a regional ocean model highlighted the strong sensitivity of upwelling dynamics to an alteration of the coastal wind stress (section 4).

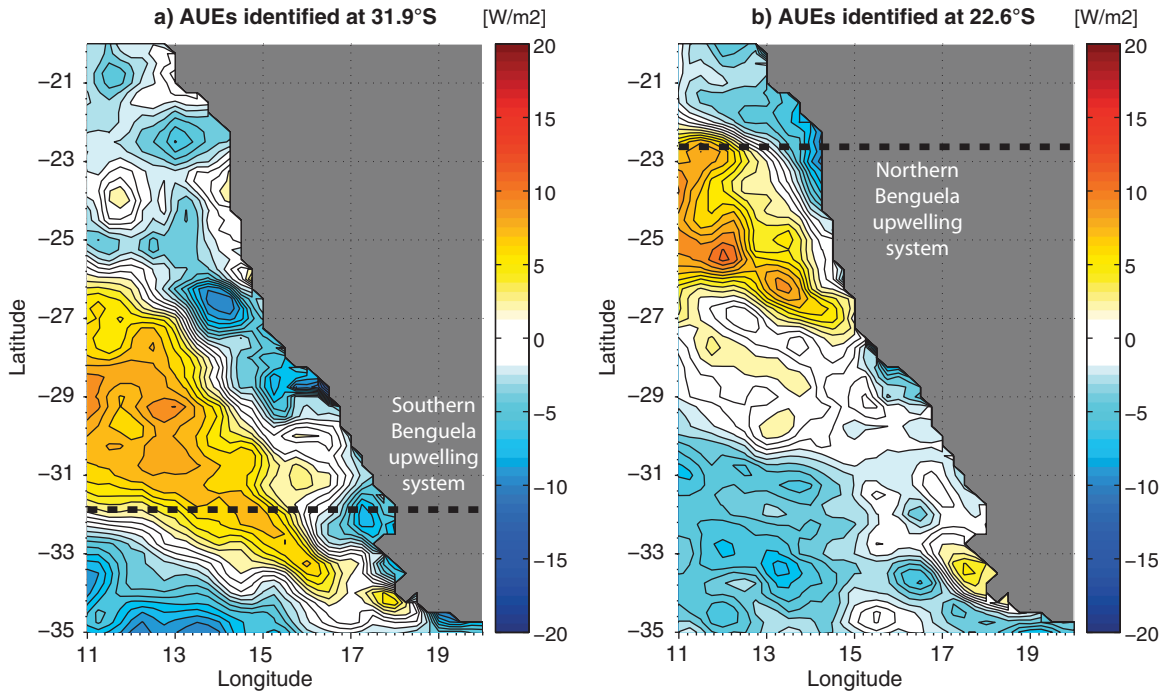

Figure 17. Composite maps of latent heat flux anomalies in the Benguela upwelling system. (a) For SUEs identified at 31.9°S. (b) For SUEs identified at 22.6°S.

[54] We analyzed the main atmospheric structures related to coastal upwelling at several latitudes along the African west coast, in both the Canary and Benguela upwelling systems. These reference latitudes were based on SST anomalies diagnosed over 2003–2009 on the continental shelf. Note that we tested an equivalent method based on SST trends (instead of SST anomalies referenced to a climatology) with the idea to adapt it later on to higher-resolution SST products for which a long-term climatology is not yet available or not easily calculable. The results obtained by both techniques proved coherent (not shown). Though the analysis based on SST trends seems to detect slightly more events, the seasonal climatology of the SUEs is very similar and the composite maps obtained for the surface wind stress resemble those presented in this study. We also want to highlight here the difficulty to catch all upwelling events with SST data only. Indeed, the technique captures the SUEs for which a surface signature is detected, which implies stratification of the column water. The SUE climatology shows a maximum of events early and late in the upwelling season because of variability in subsurface temperature gradients. Furthermore, we checked that cooling resulting from either Ekman pumping or vertical mixing could be of the same order of magnitude and, therefore, contribute to our identification of short-lived upwelling events.

[55] We depicted some wind mechanisms, and especially the alongshore wind stress component and the wind stress curl, that affect short-term SST variability at specific latitudes in each of the two upwelling systems, keeping in mind that the increased wind stress curl over an anomalous cold tongue of SST can be interpreted, in turn, as a coupling process [*Jin et al.*, 2009]. The Canary system can be split into two subregions. North of 22°N, wind-induced SUEs are related to strong wind gusts, with a remote origin and without pronounced seasonal variability. The trade winds are channeled by the Canary Islands and produce strong negative meridional wind stress anomalies, together with a positive wind stress curl favorable to upwelling conditions along the coast of Mauritania and Morocco. South of 22°N, the triggering process of SUEs is the strengthening of the trade winds perturbations offshore Cape Blanc that induces cyclonic, upwelling-favorable wind stress curl leeward of the cape at 21°N. The SUEs off Senegal show strong seasonality, with a relaxation period that corresponds to the reduction of the alongshore wind stress component. Short-term variability of the trade winds adds to the seasonal cycle of their intensity and induces short-lived cold SST anomalies at Cape Blanc.

[56] In the Benguela upwelling system, the climatology found for the SUEs is coherent with the published literature. Southern summer (December–March) is the season for coastal cold events over the whole system. The physical mechanisms driving the SST evolution are somewhat identical at all latitudes. Wind acceleration, with a strong positive anomaly of its alongshore component, leads to coastal cold upwelling. These wind bursts also induce negative wind stress curl over the shelf. The targeted study of Benguela subregions brings in clear dissociation of the Southern and Northern Benguela variability. Only a negligible number of SUEs are common to both domains. This result is consistent with other studies [*Agenbag and Shannon*, 1988; *Shannon et al.*, 2004; *Duncombe Rae*, 2005] and confirms the effect of ecological, chemical and physical barrier played by the northern edge of the Lüderitz cell at 24.5°S. This result is also confirmed by multivariate Singular Value Decomposition analyses between wind stress and SST anomalies (not shown). The main mode of covariance

clearly separates the two subregions, with asynchronous covariance variability between the Southern and the Northern Benguela region. The alternation of Northern and Southern Benguela SUEs requires more thorough investigation, and should consider the oscillation of the core of high atmospheric pressure over the open ocean as suggested by *Tyson* [1986] for the Benguela upwelling system, and by *Wooster et al*. [1976] for the Canary upwelling system.

[57] In the context of intense air-sea interactions, especially in upwelling areas, it seems useful to link wind and SST short-term variability through the analysis of the surface heat fluxes. We use here, the turbulent fluxes produced by *Bentamy et al*. [2013] on the basis of the new QS25 product and counted positive upward. As no surprise, patterns of sensible heat fluxes during cold events in the Benguela upwelling system are closely related to the SST anomalies presented in Figure 14 because the main source of variability is the air-sea temperature difference. Therefore, the sensible heat flux contributes to reduce the cooling effect of SUEs (not shown). More interestingly, composite fields of latent heat flux anomalies during SUEs (Figure 17) emphasize the competing effect of cold SST and strong winds on this energy exchange. Indeed, over a large band of colder waters (Figure 14a) and intensified winds (Figure 13b), latent heat flux anomalies show complex patterns with fine scales (Figure 17a). Offshore, positive anomalies suggest that the effect of stronger winds overcomes the reduction of evaporation otherwise expected over a colder SST. Closer to the shore and to the most significant negative SST anomalies, latent heat flux anomalies are locally negative (i.e., less evaporation) and the total turbulent heat flux (i.e., the sum of the latent and sensible heat components) appears as a damping for cooling processes over SUE time scales.

[58] At the shoreline, we studied the effect of an orographic wind dropoff on the coastal upwelling dynamics with numerical sensitivity experiments. The derivation of a realistic coastal wind dropoff from satellite observations is an almost impossible task first because a blind zone at the coast, second because the horizontal scales of pure orographic effects (a few tens of kilometers) are finer than the actual resolution of the satellite-derived product (~75 km). To offset this difficulty, we used the zonal gradient of the ECMWF meridional wind stress component to add a coastal correction to the QS25 product from its first missing value in the coastal ocean up to the shoreline. We admit that the scales of the wind dropoff are only crudely accounted by the ECMWF product used for this study. Nevertheless, the correction may be interpreted at least partially as an orographic-induced wind dropoff: the latest ECMWF outputs (available at 16 km resolution) showed that the resolution of the analysis is not an obstacle to the reproduction of the deceleration though of course with a cross-shore scale in this study larger than in the high-resolution outputs. Our sensitivity studies show that the coastal SST is always warmed when the equivalent of a dropoff is introduced. Thus, and as obtained by *Renault et al*. [2012] in their study of the central Chile upwelling system, the characteristic length scale of the coastal Ekman transport results shorter than the scale of the wind dropoff. However, no conclusive result could be obtained about the sensitivity of the dynamical response of the ocean to the structure of the shelf, mainly because the sea level is also modified by advection. After a short integration time (O(1 h)), the model sea level differences between twin experiments were usually confined at the coast. At a few latitudes, for instance around 27.5°S, 25°S, and between 23°S and 21°S, the offshore expansion of the anomaly appeared slightly larger. This meridional contrast is roughly in line with the local geometry of the inner shelf: the more gentle the local continental slope, the broader the anomaly. However, no immediate linear relationship could be diagnosed between the number of model grid points covered by the sea level anomaly and the inverse of the slope. The rich variability of the wind stress and changes in the orientation of the coast are indeed likely to complicate an interpretation after the strict manner of *Estrade et al*. [2008].

Appendix A

[59] Under the assumption of a well-mixed surface layer with temperature and thickness equal to T_{ml} and H_{ml}, respectively, lying over a constant stratification T_z, an increase of the surface wind curl will cool the SST by the quantity ΔSST knowing that

$$(T_{\mathrm{ml}} + \Delta\mathrm{SST})H_{\mathrm{ml}} = \int_0^{H^{\mathrm{ml}}-\Delta z} T_{\mathrm{ml}}\,\mathrm{d}z + \int_0^{\Delta z}\{T_{\mathrm{ml}} + (T_{\mathrm{ml}} - \Delta z T_z)\}/2\,\mathrm{d}z$$

which gives:

$$\Delta\mathrm{SST} = -\Delta z^2 T_z/(2H_{\mathrm{ml}}) \tag{A1}$$

where Δz is simply the product of the vertical pumping velocity and time (Δt):

$$\Delta z = (\rho_0 f \delta x)^{-1}\Delta\tau\Delta t \tag{A2}$$

where $\Delta\tau$ and δx are the wind stress increase and its characteristically length scale, respectively, and where we neglect meridional variations of f, the Coriolis parameter. In this approach, the depth of the surface mixed layer is fixed and chosen equal to the Ekman depth, and the mixing of the surface and deeper waters is assumed immediate and complete over the surface mixed layer.

[60] Conversely, the increase of the wind stress may be used to deepen the surface mixed layer. We assume that vertical homogenization of temperature over the new extent of the surface mixed layer is instantaneous so that the resulting cooling corresponds to the perfect mixing of T_{ml} waters (over depth H_{ml}) and colder waters with gradient T_z (over ΔH_{ml}). The new temperature of the surface mixed layer, $T_{\mathrm{ml}} + \Delta\mathrm{SST}$, now satisfies the following equation:

$$(T_{\mathrm{ml}} + \Delta\mathrm{SST})(H_{\mathrm{ml}} + \Delta H_{\mathrm{ml}}) = \int_0^{H^{\mathrm{ml}}} T_{\mathrm{ml}}\,\mathrm{d}z + \int_0^{\Delta z}\{T_{\mathrm{ml}} + (T_{\mathrm{ml}} - \Delta z T_z)\}/2\,\mathrm{d}z$$

which gives:

$$\Delta \mathrm{SST} = -(\Delta H_{\mathrm{ml}})^2 T_z / \{2\,(H_{\mathrm{ml}} + \Delta H_{\mathrm{ml}})\} \tag{A3}$$

[61] We can estimate the potential energy variation associated with this homogenization. The initial and final values referenced to the bottom of the deepened mixed layer are:

$$\int_0^{\Delta H\mathrm{ml}} \{\rho_0 - (\Delta H_{\mathrm{ml}} - z)\rho_z\} g\, z\, \mathrm{d}z + \int_{\Delta H\mathrm{ml}}^{\Delta H\mathrm{ml}+\mathrm{Hml}} \rho_0 g\, z\, \mathrm{d}z$$
$$\int_0^{\Delta H\mathrm{ml}+\mathrm{Hml}} (\rho_0 + \Delta\rho) g\, z \mathrm{d}z$$

where the stratification, ρ_z, is chosen to depend only on temperature:

$$N^2 = -g\rho_0^{-1}\rho_z \approx \mathrm{g}\,\rho_0^{-1}\alpha T_z$$

[62] Therefore, $\Delta\rho \approx -\alpha\ \Delta\mathrm{SST}$ and $\rho_z \approx -\alpha\ T_z$, and the variation in potential energy is:

$$\Delta E_p = -(\alpha/6) g (3\,\Delta H_{\mathrm{ml}}{}^2 \Delta\mathrm{SST} + 6\,\Delta H_{\mathrm{ml}}\,\Delta\mathrm{SST}\,H_{\mathrm{ml}} + 3\,\Delta\mathrm{SST}\,H_{\mathrm{ml}}{}^2 + \Delta H_{\mathrm{ml}}{}^3 T_z)$$

[63] Substituting ΔSST with equation (A3) results in:

$$\Delta E_p = (\alpha/12) g\,\Delta H_{\mathrm{ml}}{}^2 (\Delta H_{\mathrm{ml}} + 3H_{\mathrm{ml}}) T_z \tag{A4}$$

[64] We assume that this increase in potential energy is entirely balanced by the input of turbulent kinetic energy (TKE = $\rho_0\ e$) at the sea surface induced by intensified air-sea interactions (i.e., stronger winds). A proportionality factor (γ) links the flux of turbulent kinetic energy into the ocean to the cube of the surface friction velocity, $u^* = \sqrt{(\tau/\rho_0)}$, though its exact value is not well known [*Gargett et al*., 1979]. Let us write the following simplified 1-D turbulent kinetic energy balance, following for instance *Blanke and Delecluse* [1993]:

$$\partial e/\partial t = \partial \mathrm{w}' e/\partial \mathrm{z} - \mathrm{dissipation} = 0,\ \mathrm{where}\ \mathrm{w}' e|_{z=0} = \gamma \mathrm{u}*^3$$

where w is the vertical velocity and primes denote turbulent fields. We assume that an increase of the wind stress, $\Delta\tau$, or equivalently $(\Delta \mathrm{u}^*) \approx (2\ \mathrm{u}^*)^{-1}\ \Delta\tau/\rho_0$, will bring extra turbulent kinetic energy over the whole mixed layer:

$$(\Delta H_{\mathrm{ml}} + H_{\mathrm{ml}})\,\Delta \mathrm{e} = \Delta t \gamma \Delta\left(\mathrm{u}*^3\right) \approx 1.5\,\Delta t \gamma \sqrt{(\tau/\rho_0)}\,(\Delta\tau/\rho_0)$$

[65] Therefore,

$$\Delta \mathrm{TKE} = 1.5\rho_0 \Delta t \gamma \sqrt{(\tau/\rho_0)}\,(\Delta\tau/\rho_0)\,(\Delta H_{\mathrm{ml}} + H_{\mathrm{ml}})^{-1} \tag{A5}$$

and the balance between potential energy increase and turbulent kinetic energy supply reads:

$$(\alpha/12) g \Delta H_{\mathrm{ml}}{}^2 (\Delta H_{\mathrm{ml}} + 3H_{\mathrm{ml}}) T_z = 1.5\rho_0 \Delta t \gamma \sqrt{(\tau/\rho_0)}\,(\Delta\tau/\rho_0)\,(\Delta H_{\mathrm{ml}} + H_{\mathrm{ml}})^{-1} \tag{A6}$$

which allows to relate an increase of the wind stress to a deepening of the mixed layer (and, therefore, its cooling via equation (A3)).

[66] Table 2 introduces the typical values we can use to derive a crude numerical application on the Benguela shelf. The Ekman pumping velocity (equation (A2)) is then equal to 5.6×10^{-5} m/s (i.e., 4.8 m/d), and the corresponding cooling after 2 days is of the order of 1°C (equation (A1)). With the same values of the parameters, the energy approach leads to a 13.6 m deepening of the surface mixed layer after 2 days (equation (A6)), which causes a 0.8°C cooling (equation (A3)). Therefore, both effects can be diagnosed of similar magnitude on the SST, which is in keeping with the results proposed by *Renault et al*. [2012].

[67] **Acknowledgments.** We thank three anonymous reviewers and the editor, Des Barton, for their extensive and valuable comments on our manuscript. The authors thank D. Croizé-Fillon and the Ifremer/CERSAT team for data processing support, and are grateful to EumetSat, JPL, KNMI, and ECMWF, for providing satellite data and numerical analyses. We thank J.-N. Thépaut, head of Data Division, Research Department at ECMWF for expert advice on ECMWF data and for providing us with the latest high-resolution gridded winds. This research is supported by CNES (Centre National d'Études Spatiales), as part of the Ifesta-Up project funded by the TOSCA (Terre, Océan, Surfaces Continentales, Atmosphère) program. Support for this study has also been provided by CNES and Ifremer for FD in the form of a PhD scholarship, by the French Centre National de la Recherche Scientifique (CNRS) for BB, and by Ifremer for AB.

References

Agenbag, J. J., and L. V. Shannon (1988), A suggested physical explanation for the existence of a biological boundary at 24°30′S in the Benguela system, *S. Afr. J. Mar. Sci.*, *6*, 119–132.

Allen, J. S. (1973), Upwelling and coastal jets in a continuously stratified ocean, *J. Phys. Oceanogr.*, *3*, 245–257.

Antonov, J. I., R. A. Locarnini, T. P. Boyer, A. V. Mishonov, and H. E. Garcia (2006), World Ocean Atlas 2005: Salinity, in *NOAA Atlas NESDIS 62*, 182 pp, U.S. Government Printing Office, Washington, D. C.

Ayina, L.-H., and A. Bentamy (2007), Une approche globale pour améliorer les données de flux turbulents estimés aide des capteurs satellites, *Télédétection*, *7*, 91–110.

Bakun, A. (1973), Coastal upwelling indices, west coast of North America, 1946–71, *NOAA Tech. Rep. NMFS SSRF-671*, 114 pp., NOAA, Seattle, Wash.

Bakun, A., and C. S. Nelson (1991), The seasonal cycle of wind stress curl in subtropical eastern boundary current regions, *J. Phys. Oceanogr.*, *21*, 1815–1834.

Bentamy, A., and J.-F. Piollé (2004), Observation des vents de surface sur les océans au moyen de mesures diffusiométriques, *Télédetection*, *4*, 125–137.

Bentamy, A., and D. Croizé-Fillon (2011), Gridded surface wind fields from Metop/ASCAT measurements, *Int. J. Remote Sens.*, *33*(6), 1729–1754, doi:10.1080/01431161.2011.600348.

Bentamy, A., D. Croizé-Fillon, and C. Perigaud (2008), Characterization of ASCAT measurements based on buoy and QuikSCAT wind vector observation, *Ocean Sci.*, *4*, 265–274.

Bentamy, A., S. A. Grodsky, J. A. Carton, D. Croizé-Fillon, and B. Chapron (2012), Matching ASCAT and QuikSCAT winds, *J. Geophys. Res.*, *117*, C02011, doi:10.1029/2011JC007479.

Bentamy, A., S. A. Grodsky, K. Katsaros, A. M. Mesta-Nuñez, B. Blanke, and F. Desbiolles (2013), Improvement in air-sea flux estimates derived from satellite observations, *Int. J. Remote Sens.*, *34*(14), 5243–5261, doi:10.1080/01431161.2013.787502.

Blanke, B., and P. Delecluse (1993), Variability of the tropical Atlantic ocean simulated by a general circulation model with two different mixed layer physics, *J. Phys. Oceanogr.*, *23*, 1363–1388.

Blanke, B., S. Speich, A. Bentamy, C. Roy, and B. Sow (2005), Modeling the structure and variability of the southern Benguela upwelling using QuikSCAT wind forcing, *J. Geophys. Res.*, *110*, C07018, doi:10.1029/2004JC002529.

Boé, J., A. Hall, F. Colas, J. C. McWilliams, X. Qu, J. Kurian, S. B. Kapnick, and H. Frenzel (2011), What shapes mesoscale wind anomalies in coastal upwelling zones?, *Clim. Dyn.*, *36*, 2037–2049, doi:10.1007/s00382-011-1058-5.

Burls, N., and C. J. C. Reason (2008), Modelling the sensitivity of coastal winds over the Southern Benguela upwelling system to different SST forcing, *J. Mar. Syst.*, *74*, 561–584.

Capet, X. J., P. Marchesiello, and J. C. McWilliams (2004), Upwelling response to coastal wind profiles, *Geophys. Res. Lett.*, *13*, L13311, doi: 10.1029/2004GL020123.

Carr, M. E. (1998), A numerical study of the effect of periodic nutrient supply on pathways of carbon in a coastal upwelling regime, *J. Plankton Res.*, *20*, 491–516.

Chang, P., and S. G. Philander (1994), A coupled ocean-atmosphere instability of relevance to the seasonal cycle, *J. Atmos. Sci.*, *51*, 3627–3648.

Chelton, D. B., M. G. Schlax, M. H. Freilich, and R. F. Milliff (2004), Satellite measurements reveal persistent small-scale features in ocean winds, *Science*, *303*, 978–983.

Chelton, D. B., M. G. Schlax, and R. M. Samelson (2007), Summertime coupling between sea surface temperature and wind stress in the California current system, *J. Phys. Oceanogr.*, *37*, 495–517.

Crosby, D. S., L. C. Breaker, and W. H. Gemmil (1993), A proposed definition for vector correlation in geophysics: Theory and application, *Oceanic Technol.*, *10*, 355–367.

Dorman, C. E., J. F. Mejia, and D. Koračin (2013), Impact of US west coastline inhomogeneity and synoptic forcing on winds, wind stress, and wind stress curl during upwelling season, *J. Geophys. Res.*, *118*, 4036–4051, doi:10.1002/jgrc.20282.

Dunbar, S., et al. (2006), *QuikSCAT Science Data Product User Manual*, version 3.0 JPL Doc. D-18053—Rev. A, 85 pp., Jet Propulsion Laboratory, Pasadena, Calif.

Duncombe Rae, C. M. (2005), A demonstration of the hydrographic partition of the Benguela upwelling ecosystem at 26°40′S, *Afr. J. Mar. Sci.*, *27*, 617–628.

ECMWF (2007), *IFS Documentation—Cy31r1 Operational Implementation. Part IV: Physical Processes*, 155 pp. [Available at http://www.ecmwf.int/research/ifsdocs/CY31r1/PHYSICS/IFSPart4.pdf.]

Enriquez, A. G., and C. A. Friehe (1995), Effects of wind stress and wind stress curl variability on coastal upwelling, *J. Phys. Oceanogr.*, *25*, 1651–1671.

Estrade, P., P. Marchesiello, A. Colin de Verdiere, and C. Roy (2008), Cross-shelf structure of coastal upwelling: A two-dimensional expansion of Ekman's theory and a mechanism for innershelf upwelling shut down, *J. Mar. Res.*, *66*, 589–616.

Fennel, W., T. Junker, M. Schmidt, and V. Mohrholz (2012), Response of the Benguela upwelling systems to spatial variations in the wind stress, *Cont. Shelf Res.*, *45*, 65–67.

Fréon, P., M. Barrange, and J. Aristegui (2009), Eastern boundary upwelling ecosystems: Integrative and comparative approaches, *Progr. Oceanogr.*, *83*, 1–14.

Gargett, A. E., T. B. Sanford, and T. R. Osborn (1979), Surface mixing layers in the Sargasso Sea, *J. Phys. Oceanogr.*, *9*, 1090–1111.

Haack, T., D. Chelton, J. Pullen, J. D. Doyle, and M. Schlax (2008), Summertime influence of SST on surface wind stress off the U.S. West Coast from the U.S. Navy COAMPS model, *J. Phys. Oceanogr.*, *38*, 2414–2437.

Hagen, E. (2000), Northwest African upwelling scenario, *Oceanogr. Acta*, *24*, 113–127.

Halpern, D. (2002), Offshore Ekman transport and Ekman pumping off Peru during the 1997–98 El Niño, *Geophys. Res. Lett.*, *29*(5), 1075, doi: 10.1029/2001GL014097.

Hardman-Moutford, N. J., A. J. Richardson, J. J. Agenbag, E. Hagen, L. Nykjaer, F. A. Shillington, and C. Villacastin (2003), Ocean climate of the South East Atlantic observed from satellite date and wind models, *Prog. Oceanogr.*, *59*, 181–221.

IPCC (2007), Climate change 2007: Impacts, adaptation and vulnerability, in *Contribution of Working Group II to the Fourth Assessment Report of the Intergovernmental Panel on Climate Change*, edited by M. L. Parry, 976 p., Cambridge Univ. Press, Cambridge, U. K.

Jin, X., C. Dong, J. Kurian, J. C. McWilliams, D. B. Chelton, and Z. Li (2009), SST-wind interaction in coastal upwelling: Oceanic simulation with empirical coupling, *J. Phys. Oceanogr.*, *39*, 2957–2970.

Lathuilière, C., V. Echevin, and M. Lévy (2008), Seasonal and intraseasonal surface chlorophyll-a: A variability along the northwest African coast, *J. Geophys. Res.*, *113*, C05007, doi:10.1029/2007JC004433363-403.

Locarnini, R. A., A. V. Mishonov, J. I. Antonov, T. P. Boyer, and H. E. Garcia (2006), World Ocean Atlas 2005: Temperature, in *NOAA Atlas NESDIS 61*, 182 pp, U.S. Government Printing Office, Washington, D. C.

Mason, E., F. Colas, J. Molemaker, A. F. Shchepetkin, C. Troupin, J. C. McWiliams, and P. Sangrà (2011), Seasonal variability of the Canary Current: A numerical study, *J. Geophys. Res.*, *116*, C06001, doi: 10.1029/2010JC006665.

Marchesiello, P., and P. Estrade (2010), Upwelling limitation by geostrophic onshore flow, *J. Mar. Res.*, *68*, 37–62, doi:10.1357/002224010793079004.

Mitchell, T. (1997), *ICA and GA Feature Extraction and Selection for Cloud Classification*, McGraw-Hill, New York.

Mittelstaedt, E. (1991), The ocean boundary along the northwest African coast: Circulation and oceanographic properties at the sea surface, *Prog. Oceanogr.*, *26*, 307–355.

Münchow, A. (2000), Wind stress curl forcing of the coastal ocean near Point Conception, California, *J. Phys. Oceanogr.*, *30*, 1265–1280.

Penven, P. (2000), A numerical study of the Southern Benguela circulation with application to fish recruitment, PhD thesis, Univ. de Bretagne Occident., Brest, France.

Pickett, M. H., and J. D. Paduan (2003), Ekman transport and pumping in the California Current based on the U.S. Navy's high-resolution atmospheric model (COAMPS), *J. Geophys. Res.*, *108*(C10), 3327, doi: 10.1029/2003JC001902.

Renault, R., B. Dewitte, P. Marchesiello, S. Illig, V. Echevin, G. Cambon, M. Ramos, O. Astudillo, P. Minnis, and J. K. Ayers (2012), Upwelling response to atmospheric coastal jets off central Chile: A modeling study of the October 2000 event, *J. Geophys. Res.*, *117*, C02030, doi:10.1029/2011JC007446.

Reynolds, R. W., T. M. Smith, C. Liu, D. B. Chelton, K. S. Casey, and M. G. Schlax (2007), Daily high-resolution-blended analyses for sea surface temperature., *J. Clim.*, *20*, 5473–5496.

Rimaud, J., S. Speich, B. Blanke, and N. Grima (2012), The exchange of Intermediate Water in the southeast Atlantic: Water mass transformations diagnosed from the Lagrangian analysis of a regional ocean model, *J. Geophys. Res.*, *117*, C08034, doi:10.1029/2012JC008059.

Roy, C., S. Weeks, M. Rouault, G. Nelson, R. Barlow, and C. van der Lingen (2001), Extreme oceanographic events recorded in the Southern Benguela during the 1999–2000 summer season, *S. Afr. J. Sci., 97*, 465–471.

Santos, F., M. deCastro, M. Gómez-Gesteria, and I. Álvarez (2005), Differences in coastal and oceanic SST warming rates along the Canary upwelling ecosystem from 1982 to 2010, *Cont. Shelf Res.*, *47*, 1–6.

Schwing, F., M. O'Farrell, J. M. Steger, and K. Baltz (1996), Coastal upwelling indexes, west coast of North America 1946-95, *NOAA Tech. Rep. NOAA-TM-NMFS-SWFSC-231*, 32 pp., NOAA, Seattle, Wash.

Shannon, L. J., J. G. Field, and C. L. Moloney (2004), Simulating anchovy-sardine regime shift in the southern Benguela ecosystem, *Ecol. Modell.*, *172*, 269–281.

Shchepetkin, A. F., and J. C. McWilliams (2005), The regional oceanic modeling system (ROMS): A split-explicit, free-surface, topography following-coordinate oceanic model, *Ocean Modell.*, *9*, 347–404, doi: 10.1016/j.ocemod.2004.08.002.

Shchepetkin, A. F., and J. C. McWilliams (2009), Correction and commentary for "Ocean forecasting in terrain-following coordinates: Formulation and skill assessment of the regional ocean modeling system" by Haidvogel et al., *J. Comput. Phys.*, *227*, 3595–3624.

Smith, W. H. F., and D. T. Sandwell (1997), Global seafloor topography from satellite altimetry and ship depth soundings, *Science*, *277*, 1956–1962, doi:10.1126/science.277.5334.1956.

Stramma, L., M. Rhein, P. Brandt, M. Dengler, C. Boning, and M. Walter (2005), Upper ocean circulation in the western tropical Atlantic in boreal fall 2000, *Deep Sea Res.*, Part I, *52*, 221–240.

Tyson, P. D. (1986), *Climatic Change and Variability in Southern Africa*, Oxford Univ. Press, Cape Town.

Van Camp, L., L. Nykjaer, E. Mittelstaedt, and P. Schlittenhardt (1991), Upwelling and boundary circulation off Northwest Africa as depicted by infrared and visible satellite observations, *Prog. Oceanogr.*, *26*, 357–402.

Veitch, J., P. Penven, and F. Shillington (2010), Modeling equilibrium dynamics of the Benguela Current System, *J. Phys. Oceanogr.*, *40*(9), 1942–1964.

Verhoef, A., and A. Stoffelen (2010), ASCAT Wind Product User Manual, Version 1.8, EUMETSAT Doc. SAF/OSI/CDOP/KNMI/TEC/MA/126, 24 pp. [Available online at http://www.knmi.nl/publications/fulltexts/ss3_pm_ascat_1.8.pdf.]

Wang, D. P. (1997), Effects of small-scale wind on coastal upwelling with application to Point Conception, *J. Geophys. Res.*, *102*, 15,555–15,566.

Wooster, W. S., A. Bakun, and D. R. McLain (1976), The seasonal upwelling cycle along the eastern boundary of the north Atlantic, *J. Mar. Res.*, *34*, 131–141.